Full-scale, three-dimensional simulation of early-stage tumor growth: The onset of malignancy

Jiangping Xu, Guillermo Vilanova[*], Hector Gomez

Departamento de Métodos Matemáticos e de Representación, Universidade da Coruña,
Campus de A Coruña, 15071, A Coruña, Spain.

Abstract

Malignant tumors have the ability to trigger the growth of new vasculature toward them through a complex process called tumor angiogenesis. These new blood vessels provide cancerous cells with sufficient nutrients for growth and a means to escape the primary tumor and invade other tissues. This paper proposes a three-dimensional model that aims at predicting how the tumor and its associated vasculature grow during the onset of malignancy. The cellular growth equations of our model are derived using the phase-field method. We use standard reaction-diffusion equations to model the transport of chemicals. The model resolves the tumor-induced vasculature explicitly, considering capillaries with a diameter of up to ~25 µm. We propose a suitable computational method based on isogeometric analysis. We present several numerical examples to test the model, including a macroscopic simulation (~1 cm^3) on a geometry taken from a histopathological image of a human colon. The proposed model naturally predicts the angiogenic switch. Our computations show realistic patterns of tumor and vascular growth.

Keywords: Vascular tumor growth, Angiogenesis, Phase-field modeling, Isogeometric analysis

---

1. Introduction

Healthy cells produce signals to control their division process. Cancer cells, however, reproduce without the normal restraints. Abnormal cells that proliferate out of control may give rise to a tumor [1, 2]. In most cases, tumors grow rapidly consuming the nutrient and oxygen delivered by pre-existing blood vessels. However, when the cancerous mass reaches approximately 2 to 3 mm^3 [3], the absence of blood vessels inside the tumor arrests the growth of the lesion. Simplifying significantly the actual biological process, we could say that those cells located at the outermost rim may still obtain nutrients and oxygen from the circulatory system through diffusion mechanisms and continue their proliferation. On the contrary, cells in deep layers of the tumor do not have access to any source of nutrients and die from starvation forming a necrotic core. There is a transition layer between the proliferating rim and the necrotic core, called hypoxic region. The level of oxygen in such region is low due to an imbalance between the oxygen consumption and supply [4, 5]. Under hypoxic conditions, cancer cells enter a temporary, dormant state. Growth at the proliferating rim and death at the necrotic core balances the global growth of the tumor. This situation may persist for years without presenting a threat to the life of the individual.

---

[*] gvilanovac@udc.es

Preprint submitted to Computer Methods in Applied Mechanics and Engineering *July 15, 2016*

Hypoxic tumor cells may be able to promote the growth of new capillaries towards them through a process known as tumor-induced angiogenesis. These cells have gained the ability to release a series of chemical substances to the extracellular matrix, generally termed tumor angiogenic factors or TAFs. Some of the most potent TAFs include vascular endothelial growth factor (VEGF), basic fibroblast growth factor (bFGF), integrins, placenta growth factor (PLGF), or thrombospondin-1 (TSP-1) [6–9]. TAFs diffuse from the tumor until they bind to the membranes of the cells that line the blood vessels, that is, endothelial cells. At this point tumor-induced angiogenesis starts and may be briefly described as follows (for a detailed explanation the reader is referred to [10–12]). Initially, TAFs alter the quiescent phenotype of endothelial cells either to a migratory or to a proliferative phenotype [13, 14]. The former, the tip endothelial cells or TECs, will lead the capillary growth, while the latter, the stalk endothelial cells or SECs, will elongate the sprout through continuous cell division. The selection between TECs or SECs is based on the lateral inhibition mechanism [15]. The first cells reached by TAFs become TECs and subsequently express a protein called delta-like ligand 4 or Dll4. This protein binds to the nearby endothelial cell Notch receptors. Notch-activated endothelial cells become stalk cells instead of tip cells when TAFs reach them. As a result, an incipient sprout starts to develop from the parent vessels. Once liberated from the vascular membrane that envelops the parent vessel, TECs spearhead the migration following gradients of TAF. To enhance the survey of their microenvironment they extend forward membrane protrusions called filopodia [16]. Behind, the capillary grows as SECs multiply rapidly. The process continues until the leading cell fuses with another vessel (anastomosis) or until the driving stimuli end. The outcome of tumor-induced angiogenesis is a new, although pathologically defective, vascular network that partially satisfies the metabolic demands of the highly-proliferative cancer cells. As a consequence, the previously small, growth-restrained tumor can now grow unbounded becoming malignant. Tumor angiogenesis plays a key role in the onset of malignancy in several solid cancers. In particular, it is critical in the growth of colorectal cancer, in which we focus in this work.

Colorectal cancer is the third most common type of cancer globally and the third leading cause of death in United States [17, 18]. Usually, this disease develops slowly, often showing no symptoms, which makes its detection difficult. Colorectal cancer incidence and death rates have decreased due to the increase of screening frequency through colonoscopy and improvement of treatments. Due to the crucial role of angiogenesis, a number treatments that target the growth of capillaries have been developed, such as bevacizumab, regorafenib, or aflibercept [19]. Moreover, colorectal cancer develops through a series of differentiated stages, as shown next, being angiogenesis an important predictor for early-stage colorectal cancer [20].

The colon and the rectum form part of the lower digestive system. Their main functions are to absorb water and nutrients from digested food, to form and store waste and to move waste out of the body. As shown in Fig. 1, the colon is made up of distinct tissue layers, which from innermost to outermost are: mucosa, submucosa, *muscularis propria* and serosa. The mucosa layer lines the lumen of the colon and is composed by a thin layer of epithelial cells, a layer of connective tissue and a thin layer of muscle. The submucosa is a connective tissue that envelops the mucosa in which blood and lymph vessels, nerves and mucous glands are embedded. The submucosa is in turn surrounded by a thick layer of muscles, the *muscularis propria*, that powers the movement of the stool through the colon. Finally, the serosa layer enwraps the colon. The main blood and lymph vessels that supply and drain wastes from the colon are located outside these layers in the mesentery. The rectum also presents concentric layered tissues analogous to those of the colon. Due to the ordered colon and rectum layered microstructure, colorectal cancer staging is commonly defined using the TNM staging system [21], where T stands for the size of the primary tumor, N for its spread to regional lymph nodes and M for the presence of distant metastases. In this system, each letter is followed by a number, such that the higher the number, the more advanced the cancer stage. Thus, in colorectal cancer, at the earliest stage of cancer, that is Tis or carcinoma *in* *situ*, the tumor is at the beginning of its development, appears as a budding shape and is confined into the mucosa layer. In the next stage, that is T1, the tumor invades the submucosa layer. At this point, the onset of malignancy, angiogenesis plays a pivotal role as it allows the tumor to spread through subsequent layers. In the next tumor stages, namely T2, T3 and T4, the tumor grows through the muscle layer, the serosa layer and into other organs, respectively. The TNM system also classifies the stages of cancer as a function of regional lymph node invasion, such that N0 indicates no invasion, N1 three or less regional lymph nodes invaded and N2 four or more invaded lymph nodes. Finally, in this system, M0 designates a non-metastasized tumor, while M1 marks the presence of distant metastases. In a more general sense, these classifications are grouped in broader stages, numbered from 0 to IV. In the insets of Fig. 1 we depict several of these stages, highlighting those related to this work. Thus, Fig. 1A shows a carcinoma *in situ* which is still within the mucosa layer. It is only when the tumor triggers angiogenesis, gets vascularized and invades the submucosa that cancer advances to a malignant stage, as shown in Fig. 1B. Thereafter, the new supply of nutrients and oxygen facilitates the invasion of outer layers (Figs. 1B-E) and the spread to other organs (Fig. 1F).

Arguably, the avascular to vascular tumor switch through angiogenesis is one of the most important events after a tumor has formed. Thus, being able to fully understand and control angiogenesis at the early-stages of cancer development may lead to effective cancer treatments. To this end, the computational mechanics community has developed in the last decades a number of mathematical models of tumor-induced angiogenesis that try to unveil key mechanisms and predict its behavior *in silico* (for a comprehensive review on this topic see [22–24]). A variety of approaches have been developed in two-dimensions, such as the works in [25] or [26], in which using the same discretized model for angiogenesis developed in [27] coupled with tumor growth they study drug delivery or glioma vascularization and invasion, respectively. Another example of a two-dimensional study is [28], where the authors study the avascular to vascular tumor transition and the formation of a necrotic core in a fully continuous model. More recently, several authors have focused in vascular tumor growth in three dimensions; see for example [29–39]. One critical difficulty of coupling tumor growth with angiogenesis in realistic problems is the scale barrier: while angiogenesis occurs almost at cellular scale, tumor dynamics takes place at the macroscale [40]. Discrete tumor models are commonly used for cell-scale systems because cellular behavior and cell-cell interactions can be incorporated into the model easily. However, their computational cost becomes prohibitive for tumors that are detectable on usual imaging modalities. Continuum models have the capability of describing tumor dynamics with much less computational effort at macroscale [30, 31, 33, 38, 39]. The scale gap between angiogenesis and tumor growth is one of the reasons why only very few models can predict the switch from avascular to vascular growth in one theory, while keeping a continuous description of capillaries. Among the numerous models for tumor angiogenesis, the work developed by Travasso et al. in [41] uses a hybrid approach that has shown promising predictive capabilities. The model features agent-based tip endothelial cell chemotactic migration coupled with continuous descriptions of tumor angiogenic factors and stalk and quiescent endothelial cells. The migration of TECs was augmented in [42] to include haptotaxis. More recently, the model was coupled with a tumor growth model to simulate the angiogenesis switch in [39, 43].

In this paper, we extend to three dimensions the model that we recently put forth in [43]. We present a suitable computational method based on isogeometric analysis that permits a simple discretization of the model equations on complex geometries. The aim of this paper is to apply the model to early-stage colorectal cancer to study the role of angiogenesis and the avascular/vascular malignant transition within the mucosa and submucosa layers. To accomplish this, we perform a three-dimensional computation on the geometry of a macroscopic piece of colon tissue taken from a histopathological image.

This paper is organized as follows: Section 2 describes the model for vascular tumor growth including the phase-field models for cellular growth and reaction-diffusion equations for soluble substances. Section

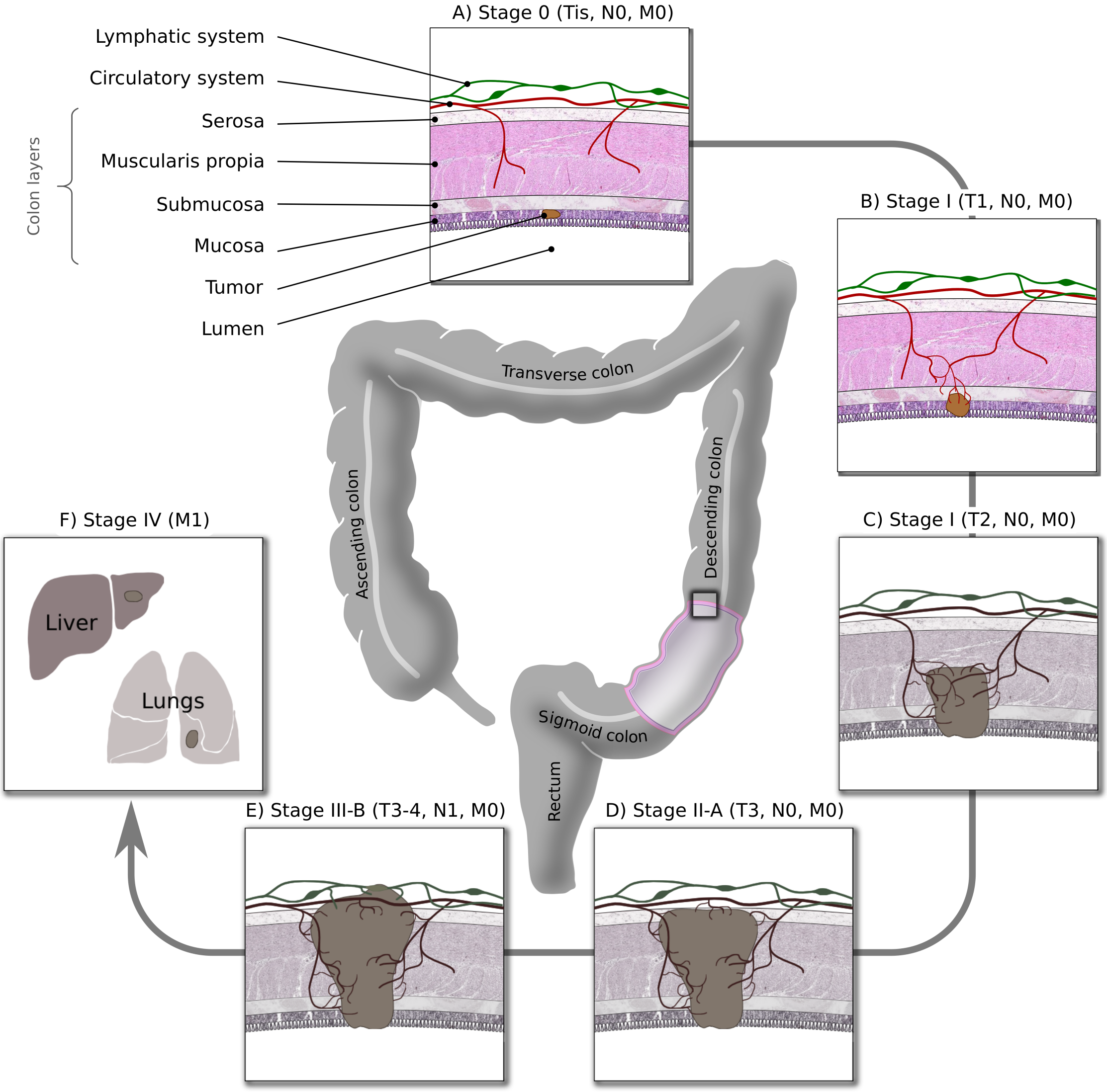

Figure 1. Staging of colorectal cancer. Colorectal cancer usually starts as a carcinoma *in situ* in the inner layer of the colon or mucosa (A). Its ability to trigger angiogenesis and to invade the adjacent submucosa layer leads to tumor malignancy (B). Afterwards, the tumor can invade other layers of the colon or rectum (C-E) and colonize distant organs (F).

3 presents the numerical method. Four numerical simulations are presented in Section 4. Finally, we draw conclusions in Section 5.

2. Coupled model for vascular tumor growth

Our model is composed of two coupled compartments; one for cellular growth and another for the transport of soluble substances in the tissue. Cellular growth is modeled using the phase-field method, while we employ standard diffusion-reaction equations to model the transport of chemicals. In what follows, we present the main equations of our model and refer the reader to Appendix A for details.

2.1. *Phase fields for cellular growth*

The phase-field method is a mathematical theory to model interface problems [44, 45]. One way to think about the phase field method is as a regularization technique to reformulate free-boundary problems as partial differential equations (PDEs) posed on a fixed domain. The key technical ingredient is to introduce a smooth function (the phase field) defined on a fixed domain that describes the interfaces implicitly. The dynamics of the phase field is controlled by an evolution equation derived from non-equilibrium thermodynamics [46]. The equation is formulated such that its solution naturally develops flat areas, associated to pure phases, and steep gradients, which represent diffuse approximations to the interfaces. The applications of the phase-field method range from solidification dynamics [47, 48], fracture mechanics [49–51], fluid–structure interaction [52, 53], crystal growth [54–56], to tumor growth [31, 32, 38, 39, 57–60]. Therefore, the interfaces may represent, for example, transitions between different phases, cracks, fluid-solid interfaces or dislocations. In tumor growth modeling, the interfaces usually represent boundaries between different cell types. For consistency with the usual nomenclature in phase-field modeling, we will also refer to these cell types as *phases*. For a recent overview of the phase-field method, the reader is referred to [61].

2.1.1. *Phase field model of tumor dynamics*

We consider cancerous and host tissue as two distinct phases which are represented by a phase field variable $\phi \in [0, 1]$. The function ϕ varies from ∼0 (host tissue) to ∼1 (tumor) developing a smooth transition layer that represents the tumor boundary. The dynamics of ϕ is controlled by the non-conserved phase-field equation

$$\frac{\partial \phi}{\partial t} = M_\phi \left(\lambda_\phi^2 \Delta \phi - \mu_\phi (\phi, \sigma) \right), \tag{1}$$

where M_ϕ is a positive function representing the tumor mobility and λ_ϕ is a length scale that defines the thickness of the diffuse interface between the tumor and the host tissue. The term μ_ϕ the derivative of a double-well potential Ψ_ϕ^{ch}, which has local minima at $\phi = 0$ and $\phi = 1$. The function μ_ϕ may be thought of as a reaction term that permits the coexistence of the tumor (corresponding to the metastable solution $\phi = 1$) and the host tissue (associated to the metastable solution $\phi = 0$). The specific form of μ_ϕ is given by

$$\mu_\phi(\phi, \sigma) = \frac{\partial \Psi_\phi^{\mathrm{ch}}}{\partial \phi}(\phi, \sigma) \quad \text{with} \quad \Psi_\phi^{\mathrm{ch}} = g(\phi) + m(\sigma)\, h(\phi) \tag{2}$$

Here, $g(\phi) = \phi^2(1 - \phi)^2$ is a symmetric double-well potential with two local minima at $\phi = 0$ and $\phi = 1$. The term $m(\sigma)h(\phi)$ introduces a non-symmetric perturbation in Ψ_ϕ^{ch} which energetically favors one of the two metastable solutions depending on the value of σ. The function $h(\phi)$ is simply a blending curve which is monotonically increasing and satisfies $h(0) = 0$, $h(1) = 1$. In addition, if Ψ_ϕ^{ch} is to have local extrema at $\phi = 0$ and $\phi = 1$, then h must verify the conditions $h'(0) = h'(1) = 0$. The simplest function satisfying these requirements is the cubic polynomial $h(\phi) = \phi^2(3 - 2\phi)$. The function $m(\sigma)$, usually called tilting function, is defined as

$$m(\sigma) = -m_{\mathrm{ref}} \arctan\left(\frac{\sigma - \sigma^{h-v}}{\sigma_{\mathrm{ref}}^m} \right). \tag{3}$$

Here, m_{ref} and σ_{ref}^m are reference values and σ^{h-v} represents the value of the nutrient concentration that defines the threshold between hypoxic and viable tumor cells. For Ψ_ϕ^{ch} to achieve local minima at $\phi = 0$

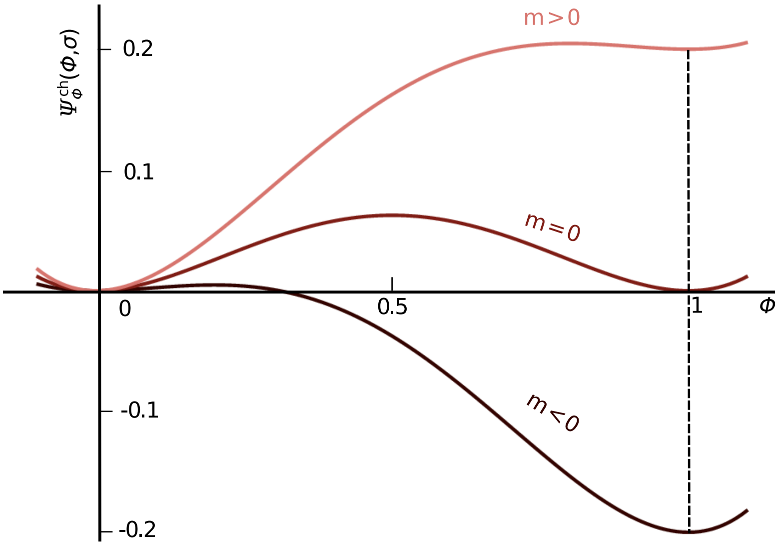

Figure 2. Double-well potential for different values of the nutrient concentration. When $\sigma < \sigma^{h-v}$, then $m > 0$ and the tumor regresses. When $\sigma > \sigma^{h-v}$, $m < 0$ and the tumor grows.

and $\phi = 1$, the function m must verify $|m(\sigma)| < 1/3$ for all σ (see [45] for details). This constraint can be satisfied simply taking $m_{\mathrm{ref}} < 2/(3\pi)$. Thus, we assume $m_{\mathrm{ref}} = 2/[(3+\epsilon)\pi]$, where ϵ is a small positive constant.

Plotting Ψ_ϕ^{ch} in Fig. 2, it may be observed that when $\sigma < \sigma^{h-v}$, $\phi = 0$ is the metastable solution with the lowest energy level, and Eq. (1) predicts tumor regression. When $\sigma > \sigma^{h-v}$, the metastable solution $\phi = 1$ has a lower energy level than $\phi = 0$ and Eq. (1) leads to tumor growth. To gain insight into the dynamics of Eq. (1), we note that by using the techniques presented in [61], it may be shown that as $\lambda_\phi \to 0$, Eq. (1) converges to a free boundary problem in which the moving boundary is the tumor/host-tissue interface. It may be proven that the normal velocity of the tumor boundary (pointing towards the healthy tissue) scales as $v_n \sim -M_\phi(\kappa + m(\sigma))$, where κ is the additive curvature of the tumor interface with the sign convention that κ is positive for a convex tumor. The curvature term tends to decrease the interfacial area, while the term $m(\sigma)$ produces tumor growth for $\sigma > \sigma^{h-v}$ ($m(\sigma) < 0$) and regression for $\sigma < \sigma^{h-v}$ ($m(\sigma) > 0$). Since $m(\sigma)$ behaves linearly in a neighborhood of σ^{h-v}, Eq. (1) encodes the usual assumption that tumor spheroids increase their radii linearly with time and nutrient concentration [62, 63].

2.1.2. Phase field model of angiogenesis

The spatial location of capillaries is described by a phase field $c \in [-1, 1]$. Where $c \approx 1$ the tissue is occupied by capillaries and $c \approx -1$ represents avascular tissue. Again, the phase field equation automatically produces a smooth transition layer between the capillaries and the surrounding tissue. Based on the work [41, 42], we describe the location of endothelial cells using the equation

$$\frac{\partial c}{\partial t} = \nabla \cdot \left(M_c \nabla \left(\mu_c(c) - \lambda_c^2 \Delta c \right) \right) + \mathcal{B}_p(f)\, c \mathcal{H}(c), \tag{4}$$

where M_c is a positive constant the represents the endothelial cell mobility, λ_c is a length scale that defines the thickness of the capillary wall, $\mathcal{H}(\cdot)$ is a smoothed-out Heaviside function[1] and $\mu_c(c) = c^3 - c$ is the derivative of the potential $\Psi_c^{\mathrm{ch}}(c) = c^4/4 - c^2/2$. Note that Ψ_c^{ch} is a symmetric double-well potential with two local minima at $c = -1$ and $c = 1$. The term $\mathcal{B}_p(f)$ represents the proliferation rate of endothelial cells as a function of TAF concentration. We define $\mathcal{B}_p(f)$ as a linear function with a plateau; see Appendix A for details.

Eq. (4) models the dynamics of stalk endothelial cells, which proliferate behind their leading tip cell [13, 16]. The migration of TECs is modeled using an agent-based model described in Appendix A. The discrete agents are integrated into the continuous formulation using the concept of templates [42]. This angiogenesis model has been shown to predict realistic capillary networks both in two and three dimensions, representing *in vitro* and *in vivo* experimental setups [64].

2.2. Transport and reactions of chemical substances

2.2.1. Tumor angiogenic factor

TAF is produced by tumor cells and is transported by diffusion through the interstitium until it reaches the capillaries, where it is consumed. We model this process using the reaction-diffusion equation

$$\frac{\partial f}{\partial t} = \nabla \cdot \left(D_f \nabla f \right) + \phi \left(1 - f\right) \mathcal{G}\left(\sigma\right) - B_u f c \mathcal{H}\left(c\right), \tag{5}$$

where f is a dimensionless variable that represents a balance between pro- and anti-angiogenic factors, D_f is the diffusion constant, B_u is the uptake rate of TAF by endothelial cells and $\mathcal{G}$ is the secretion rate of TAF by tumor cells. Denoting by σ^{n-h} the value of the nutrient concentration that defines the threshold between necrotic and hypoxic tumor cells, we define $\mathcal{G}$ as a hill function of σ that achieves a maximum at $\sigma = (\sigma^{n-h} + \sigma^{h-v})/2$ and decreases quickly away from this value. This functional form reflects the experimentally-proven fact that TAF is mainly released by hypoxic tumor cells.

2.2.2. Nutrient

The growth of a tumor depends on the nutrients that are available in its microenvironment. These nutrients include oxygen, glucose, amino acids and fatty acids. They are carried by the circulatory system and released in capillary beds. Thereafter, they diffuse reaching the tissue which is up to ~200 µm away from the release point. In our model, we consider only one vital nutrient σ, which is assumed to be the limiting growth factor for tumor development. For simplicity, we associate σ to dimensionless measure of oxygen. Taking into account that nutrients are supplied by capillaries and consumed by tumor and host cells at different rates, we model this process by the reaction-diffusion equation

$$\frac{\partial \sigma}{\partial t} = \nabla \cdot (D_\sigma \nabla \sigma) + V_p^c (1 - \sigma) c \mathcal{H}(c) \mathcal{S} - V_u^T \sigma \phi - V_u^H \sigma \mathcal{H}(1 - \phi), \tag{6}$$

where D_σ is the nutrient diffusion constant, V_p^c is the nutrient release rate, while V_u^T and V_u^H are the uptake rates of nutrient by cancerous and non-cancerous tissue, respectively. Experimental evidence shows that $V_u^T >> V_u^H$ [65]. The consumption term $V_u^H \sigma \mathcal{H}(1 - \phi)$ implicitly assumes that the host tissue and the capillaries have the same uptake rate of nutrient. In the source term $V_p^c(1 - \sigma) c \mathcal{H}(c) \mathcal{S}$, the dimensionless quantity $\mathcal{S}$ is a crude measure of the functionality of the capillary network. It is known that tumor-induced

---

[1] We use a hyperbolic tangent approximation of the Heaviside function to increase the convergence rate of our Newton-Raphson nonlinear solver.

capillary networks are aberrant, highly disorganized and less efficient than physiological vasculature in terms of tissue oxygenation. Modeling blood flow and oxygen transportation in capillary beds in an open scientific problem even in physiological conditions and it is out of the scope of this paper. However, it has been experimentally verified that the oxygen delivery rate decreases when the vascular density increases beyond a certain threshold [66]. It may be shown that for a capillary network composed of n_c capillaries with lengths $\{l_i\}_{i=1,\ldots,n_c}$, such that $l_{\max} = \max_{i=1,\ldots,n_c}\{l_i\}$, the vascular density scales as $\rho_v \sim l_{\max}^{-2} R \sum_{i=1}^{n_c} l_i$ in three dimensions and $\rho_v \sim l_{\max}^{-1} \sum_{i=1}^{n_c} l_i$ in two dimensions. Therefore, as a first approximation, we take $\mathcal{S} = \rho_v^{-1}$. A similar expression was used in a experimental study of tumor angiogenesis to characterize a capillary network [67].

3. Numerical method

This section presents the proposed numerical algorithm to solve the governing equations of our model. Eqns. (1)–(6) are time-dependent, nonlinear PDEs which involve fourth-order spatial differential operators. In addition, the solution to the equations exhibits small-scale features, including thin layers that move throughout the domain. Since our goal is to solve the equations on three-dimensional domains at the tissue scale, we need to introduce efficient time and space discretizations. To perform the space discretization, we make use of isogeometric analysis (IGA), originally introduced in [68] and further studied in [69–71]. The main idea of IGA is to use blending functions of Computer Aided Design, e.g., non-uniform rational B-splines (NURBS) and the isoparametric concept for the numerical solution of PDEs. IGA may be used to discretize PDEs in weak [72] or strong form [73–75]. An important property of IGA that has been recently proven is that Galerkin solutions can be obtained with only one evaluation per degree of freedom using the concept of variational collocation [76]. However, the most important feature of IGA for this paper is that it permits straightforward discretization of fourth-order differential operators through the use of globally C^1-continuous splines. IGA has also shown remarkable robustness and stability in phase-field problems (see, e.g., [77–79]), which makes it a suitable technique for our model equations. The time integration of phase-field equations also poses significant challenges due to the lack of convexity of the potentials Ψ_ϕ^{ch} and Ψ_c^{ch}, which produces uphill diffusion in localized areas of the domain [80, 81]. We integrate in time using the generalized-α method [82].

3.1. Strong form of the equations

Let $\Omega \subset \mathbb{R}^d$, where $d = 2$ or 3, be the computational domain that represents a macroscopic ($\sim$1 cm^3) piece of tissue. The domain Ω is fixed in time. The set Γ denotes the boundary of Ω and is supposed to have a well-defined unit outward normal $\boldsymbol{n}$. We will analyze the time interval $\mathcal{I} = (0, T)$. The problem can be stated as: Given suitable initial conditions, find ϕ, c, f and σ such that

$$\frac{\partial \phi}{\partial t} = M_\phi \left(\lambda_\phi^2 \Delta \phi - \mu_\phi(\phi, \sigma) \right) \quad \text{in} \quad \Omega \times (0,T), \tag{7}$$

$$\frac{\partial c}{\partial t} = \nabla \cdot \left(M_c \nabla \left(\mu_c\left(c\right) - \lambda_c^2 \Delta c \right) \right) + \mathcal{B}_p\left(f\right) c \mathcal{H}\left(c\right) \quad \text{in} \quad \Omega \times (0,T), \tag{8}$$

$$\frac{\partial f}{\partial t} = \nabla \cdot \left(D_f \nabla f \right) + \phi \left(1 - f\right) \mathcal{G}\left(\sigma\right) - B_u f c \mathcal{H}\left(c\right) \quad \text{in} \quad \Omega \times (0,T), \tag{9}$$

$$\frac{\partial \sigma}{\partial t} = \nabla \cdot (D_\sigma \nabla \sigma) + V_p^c (1 - \sigma) c \mathcal{H}(c) \mathcal{S} - V_u^T \sigma \phi - V_u^H \sigma \mathcal{H}(1 - \phi) \quad \text{in} \quad \Omega \times (0,T), \tag{10}$$

$$\nabla \phi \cdot \boldsymbol{n} = 0 \quad \text{on} \quad \Gamma \times (0,T), \tag{11}$$

$$\nabla \left(\mu_c(c) - \lambda_c^2 \Delta c \right) \cdot \boldsymbol{n} = 0 \quad \text{on} \quad \Gamma \times (0,T), \tag{12}$$

$$\Delta c = 0 \quad \text{on} \quad \Gamma \times (0,T), \tag{13}$$

$$\nabla f \cdot \boldsymbol{n} = 0 \quad \text{on} \quad \Gamma \times (0,T), \tag{14}$$

$$\nabla \sigma \cdot \boldsymbol{n} = 0 \quad \text{on} \quad \Gamma \times (0,T). \tag{15}$$

Note that the boundary conditions (11)–(15) are compatible with the mass conservation and energy dissipation properties of the individual equations. We note that the field c is not only governed by Eq. (8), but it is also updated dynamically to account for the migration of TECs. The discrete updates are seamlessly integrated in the continuous description using the concept of templates. In reference [42], we described in detail the algorithms to couple the continuous and discrete compartments in the context of an angiogenesis model without tumors and nutrients. The ideas carry over to the coupled model, so we omit the details here.

3.2. Galerkin form

Let us define the functional space $\mathcal{V} \subset \mathcal{H}^2(\Omega)$, where $\mathcal{H}^2(\Omega)$ is the Sobolev space of square integrable functions with square integrable first and second derivatives in the domain Ω. To perform space discretization we introduce the finite-dimensional space $\mathcal{V}^h \subset \mathcal{V}$, where $\mathcal{V}^h = \text{span}\{N_A\}_{A=1,\dots,n_b}$. The N_A's are linearly independent, which implies that the dimension of $\mathcal{V}^h$ is n_b. We define the functions N_A by mapping into the domain Ω globally C^1-continuous splines defined on a parametric space. The mapping is performed using the isoparametric concept. For non-singular mappings this procedure ensures global C^1-continuity of the discrete solution in physical space, which guarantees that the requirement $\mathcal{V}^h \subset \mathcal{H}^2(\Omega)$ is satisfied. The space of weighting functions will be also $\mathcal{V}^h$, giving rise to a Galerkin formulation. We define discrete approximations to the problem's solution denoted by ϕ^h, c^h, f^h and σ^h. Their corresponding weighting functions are w_ϕ^h, w_c^h, w_f^h and w_σ^h. The Galerkin formulation of the problem can be stated as: Find $\{\phi^h, c^h, f^h, \sigma^h\} \in \mathcal{V}^h$ such that for all $\{w_\phi^h, w_c^h, w_f^h, w_\sigma^h\} \in \mathcal{V}^h$:

$$\left(w_\phi^h, \frac{\partial \phi^h}{\partial t} \right)_\Omega + \left(\nabla w_\phi^h, M_\phi \lambda_\phi^2 \nabla \phi^h \right)_\Omega + \left(w_\phi^h, M_\phi \mu_\phi(\phi^h, \sigma^h) \right)_\Omega = 0 \tag{16}$$

$$\left(w_c^h, \frac{\partial c^h}{\partial t} \right)_\Omega + \left(\nabla w_c^h, M_c \nabla \mu_c(c^h) \right)_\Omega + \left(\Delta w_c^h, M_c \lambda_c^2 \Delta c^h \right)_\Omega - \left(w_c^h, \mathcal{B}_p\left(f^h\right) c^h \mathcal{H}\left(c^h\right) \right)_\Omega = 0 \tag{17}$$

$$\left(w_f^h, \frac{\partial f^h}{\partial t} \right)_\Omega + \left(\nabla w_f^h, D_f \nabla f^h \right)_\Omega + \left(w_f^h, B_u f^h c^h \mathcal{H}\left(c^h\right) \right)_\Omega - \left(w_f^h, \phi^h (1 - f^h) \mathcal{G}(\sigma^h) \right)_\Omega = 0 \tag{18}$$

$$\left(w_\sigma^h, \frac{\partial \sigma^h}{\partial t} \right)_\Omega + \left(\nabla w_\sigma^h, D_\sigma \nabla \sigma^h \right)_\Omega + \left(w_\sigma^h, V_u^T \sigma^h \phi^h + V_u^H \sigma^h \mathcal{H}(1 - \phi^h) - V_p^c (1 - \sigma^h) c^h \mathcal{H}\left(c^h\right) \mathcal{S} \right)_\Omega = 0 \tag{19}$$

where $(\cdot,\cdot)_\Omega$ is the L^2 inner product with respect to the domain Ω. The discrete solution ϕ^h is defined as

$$\phi^h(\boldsymbol{x},t) = \sum_{A=1}^{n_b} \phi_A(t)\, N_A(\boldsymbol{x})\,. \tag{20}$$

In Eq. (20), the ϕ_A's are the so-called control variables [68], which constitute the unknowns of the problem. The discrete solutions c^h, f^h and σ^h are defined similarly. The weight function w^h_ϕ is fixed in time and can be expressed as

$$w^h_\phi(\boldsymbol{x}) = \sum_{A=1}^{n_b} w_{\phi,A}\, N_A(\boldsymbol{x})\,. \tag{21}$$

The weight functions w^h_c, w^h_f and w^h_σ are defined analogously.
Remark: Note that the condition $\mathcal{V}^h \subset \mathcal{H}^2(\Omega)$ is necessary for the Galerkin formulation to be well defined due to the presence of second-order derivatives in the variational formulation; see the third term in Eq. (17).

3.3. Time discretization

The above Galerkin formulation is discretized in time using the generalized-α method, which is second-order accurate and unconditionally A-stable [82]. The time interval of interest, namely $(0,T)$, is discretized into N sub-intervals $I_n = (t_n, t_{n+1})$, $n = 0,1,\ldots,N-1$, where $0 = t_0 < t_1 < \cdots < t_{N-1} < t_N = T$. The time step is $\Delta t_n = t_{n+1} - t_n$. Let us call ϕ^h_n the time discrete approximation to $\phi^h(\cdot,t_n)$. Similarly, we define c^h_n, f^h_n and σ^h_n. The global vectors of control variables associated to ϕ^h_n, c^h_n, f^h_n and σ^h_n are denoted, respectively, $\boldsymbol{\Phi}_n$, $\boldsymbol{C}_n$, $\boldsymbol{F}_n$, $\boldsymbol{\Sigma}_n$, while their time derivatives are written as $\dot{\boldsymbol{\Phi}}_n$, $\dot{\boldsymbol{C}}_n$, $\dot{\boldsymbol{F}}_n$, $\dot{\boldsymbol{\Sigma}}_n$. Using this notation, we define the residual vector

$$\boldsymbol{R}(\dot{\boldsymbol{S}}_n, \boldsymbol{S}_n) = \{\boldsymbol{R}_A(\dot{\boldsymbol{S}}_n, \boldsymbol{S}_n)\}_{A=1,\ldots,n_b} \tag{22}$$

where

$$\boldsymbol{R}_A(\dot{\boldsymbol{S}}_n, \boldsymbol{S}_n) = \left\{ \begin{array}{c} R^\phi_A \\ R^c_A \\ R^f_A \\ R^\sigma_A \end{array} \right\}, \quad \boldsymbol{S}_n = \left\{ \begin{array}{c} \boldsymbol{\Phi}_n \\ \boldsymbol{C}_n \\ \boldsymbol{F}_n \\ \boldsymbol{\Sigma}_n \end{array} \right\} \tag{23}$$

and

$$R^\phi_A = \left(N_A, \dot{\phi}^h_n\right)_\Omega + \left(\nabla N_A, M_\phi \lambda^2_\phi \nabla \phi^h_n\right)_\Omega + \left(N_A, M_\phi \mu_\phi(\phi^h_n, \sigma^h_n)\right)_\Omega \tag{24}$$

$$R^c_A = \left(N_A, \dot{c}^h_n\right)_\Omega + \left(\nabla N_A, M_c \nabla \mu_c(c^h_n)\right)_\Omega + \left(\Delta N_A, M_c \lambda^2_c \Delta c^h_n\right)_\Omega - \left(N_A, \mathcal{B}_p\left(f^h_n\right) c^h_n \mathcal{H}\left(c^h_n\right)\right)_\Omega \tag{25}$$

$$R^f_A = \left(N_A, \dot{f}^h_n\right)_\Omega + \left(\nabla N_A, D_f \nabla f^h_n\right)_\Omega + \left(N_A, B_u f^h_n c^h_n \mathcal{H}\left(c^h_n\right)\right)_\Omega - \left(N_A, \phi^h_n(1 - f^h_n)\mathcal{G}(\sigma^h_n)\right)_\Omega \tag{26}$$

$$R^\sigma_A = \left(N_A, \dot{\sigma}^h_n\right)_\Omega + \left(\nabla N_A, D_\sigma \nabla \sigma^h_n\right)_\Omega + \left(N_A, V^T_u \sigma^h_n \phi^h_n + V^H_u \sigma^h_n \mathcal{H}(1 - \phi^h_n) - V^c_p(1 - \sigma^h_n) c^h_n \mathcal{H}\left(c^h_n\right) \mathcal{S}\right)_\Omega \tag{27}$$

The time integration scheme may be written as: Given $\boldsymbol{S}_n$, $\dot{\boldsymbol{S}}_n$ and Δt_n, find $\boldsymbol{S}_{n+1}$ and $\dot{\boldsymbol{S}}_{n+1}$ such that

$$\boldsymbol{R}(\dot{\boldsymbol{S}}_{n+\alpha_m}, \boldsymbol{S}_{n+\alpha_f}) = 0 \tag{28}$$

where

$$\dot{\boldsymbol{S}}^h_{n+\alpha_m} = \dot{\boldsymbol{S}}^h_n + \alpha_m \left(\dot{\boldsymbol{S}}^h_{n+1} - \dot{\boldsymbol{S}}^h_n\right) \tag{29}$$

$$\boldsymbol{S}^h_{n+\alpha_f} = \boldsymbol{S}^h_n + \alpha_f \left(\boldsymbol{S}^h_{n+1} - \boldsymbol{S}^h_n\right) \tag{30}$$

$$\boldsymbol{S}^h_{n+1} = \boldsymbol{S}^h_n + \Delta t_n \dot{\boldsymbol{S}}^h_n + \gamma \Delta t_n \left(\dot{\boldsymbol{S}}^h_{n+1} - \dot{\boldsymbol{S}}^h_n\right) \tag{31}$$

Here, α_m, α_f and γ are real-valued parameters that define the accuracy and stability of the method. We take the values

$$\alpha_m = \frac{1}{2}\left(\frac{3-\rho_\infty}{1+\rho_\infty}\right); \quad \alpha_f = \frac{1}{1+\rho_\infty}; \quad \gamma = \frac{1}{2} + \alpha_m - \alpha_f \quad \text{where} \quad \rho_\infty = 1/2. \tag{32}$$

This choice guarantees second-order accuracy and unconditional A-stability [82].

Eq. (28) constitutes an algebraic nonlinear system that needs to be solved at each time step. We use the Newton-Raphson method with consistent tangent matrix. Note that $\dot{\boldsymbol{S}}_{n+\alpha_m}$ and $\boldsymbol{S}_{n+\alpha_f}$ are, apparently, two different unknowns, but Eqns. (29)–(31) may be used to reduce them to just one unknown vector of control variables, for example, $\dot{\boldsymbol{S}}_{n+1}$. Here, this set of control variables is also used to linearize the equations. The algorithm may be summarized as follows: Given the initial guesses $\boldsymbol{S}_{n+1,(0)} = \boldsymbol{S}_n$ and $\dot{\boldsymbol{S}}_{n+1,(0)} = (\gamma-1)\dot{\boldsymbol{S}}_n/\gamma$, which are compatible with Eq. (31), compute $\Delta\dot{\boldsymbol{S}}_{n+1,(i)}$ from the linearized equation

$$\boldsymbol{R}\left(\dot{\boldsymbol{S}}^{(i)}_{n+\alpha_m}, \boldsymbol{S}^{(i)}_{n+\alpha_f}\right) + \frac{\partial \boldsymbol{R}}{\partial \dot{\boldsymbol{S}}_{n+1}}\left(\dot{\boldsymbol{S}}^{(i)}_{n+\alpha_m}, \boldsymbol{S}^{(i)}_{n+\alpha_f}\right)\Delta\dot{\boldsymbol{S}}^{(i)}_{n+1} = 0 \tag{33}$$

and update the control variables maintaining compatibility with Eq. (31), as

$$\dot{\boldsymbol{S}}^{(i)}_{n+1} = \dot{\boldsymbol{S}}^{(i-1)}_{n+1} + \Delta\dot{\boldsymbol{S}}^{(i)}_{n+1} \tag{34}$$

$$\boldsymbol{S}^{(i)}_{n+1} = \boldsymbol{S}^{(i-1)}_{n+1} + \gamma \Delta t_n \Delta\dot{\boldsymbol{S}}^{(i)}_{n+1} \tag{35}$$

The superindex (i) in Eqns. (34)–(35) indicates the Newton-Raphson iteration. This iterative process must be repeated until the residual is reduced to a tolerance $\Upsilon_{\text{N-R}}$ of its initial value within a time step. For a multiphysics problem like the one considered here, it is important not to check only the convergence of the global residual vector $\boldsymbol{R}$, but also its components corresponding to each variable due to the potentially different scaling of the equations that may lead to false convergence. We have converged the individual residuals $\boldsymbol{R}_\phi$, $\boldsymbol{R}_c$, $\boldsymbol{R}_f$ and $\boldsymbol{R}_\sigma$ up to a tolerance $\Upsilon_{\text{N-R}} = 10^{-2}$. Using lower values of $\Upsilon_{\text{N-R}}$ did not produce noticeable changes in the solution.

4. Numerical results

In this section we present and discuss four numerical simulations that aim at reproducing *in vitro* and *in vivo* experiments. Each simulation starts with a small tumor. The phase field describing cancerous cells, ϕ, is zero everywhere in the domain, except inside the tumor, where $\phi = 1$. The tumoral tissue is classified as proliferative, hypoxic and necrotic based on the nutrient concentration. The necrotic region is the area of the tumor where $\sigma < \sigma^{n-h}$. The hypoxic region is defined by the condition $\sigma \in (\sigma^{n-h}, \sigma^{h-v})$ and the proliferative region is the area of the tumor that verifies $\sigma > \sigma^{h-v}$.

As we are modeling the onset of malignancy of the tumors, the simulations start from the point when cancer cells have already gained the ability to trigger angiogenesis. With the goal of representing this scenario realistically, we adopt the following assumptions: We place at least one pre-existing capillary within the computational domain, where the initial value of c is 1; elsewhere in the tissue we take $c = -1$. Each capillary acts as a source of oxygen, thus, we start with the maximum level of nutrient inside them, $\sigma = 1$. In the necrotic region, which is located deep inside the tumor, we initially take $\sigma = 0$. Everywhere else in the tissue, we take $\sigma = \sigma^0_{\mathrm{ecm}}$ as initial condition. σ^0_{ecm} is a constant value representing a physiological nutrient concentration which is larger than σ^{h-v}. Unless otherwise stated, we take $\sigma^0_{\mathrm{ecm}} = 0.45$. We suppose that at the beginning of the simulation there is no TAF in the tissue except inside the tumor, where we take $f = 0.1$. The simulations are performed using the parameters defined in Table A.1 and the boundary conditions (11)–(15), except when otherwise specified.

We open this section with a three-dimensional simulation of tumor growth and angiogenesis in a simple geometric domain that may represent an *in vitro* experiment. We consider a spherical tumor near a curved capillary, both within a tissue of cubic shape. We use this example to test our model and algorithms without the inconveniences of complex geometries. Then, we perform simulations using the geometry of a section of a human colon extracted from an image. We analyze this example using two- and three-dimensional domains. Finally, inspired by a recent experiment [83], we investigate the disappearance of the necrotic regions of small tumor spheroids in a three-dimensional setting.

4.1. Coupled tumor growth and angiogenesis on a cubic domain

We perform the simulation on a cubic portion of tissue with side 2025 µm. At the center of the domain, we place a spherical tumor. As shown on the top left panel of Fig. 3a, we exploit the symmetry of this configuration and perform our simulation on one octant of the cube, using a uniform computational mesh composed by 128^3 C^1-quadratic elements. The radius of the initial tumor (brown) is $R_t = 625\,\mu\mathrm{m}$. We assume that, initially, the tumor has a concentric spherical necrotic core with a radius $R_n = 0.45 R_t$. We also place in the domain an initial tubular capillary (red) with radius 25 µm. This vessel acts as a source of nutrient and as the parent capillary for tumor-induced angiogenesis.

Fig. 3 shows the numerical results. Fig. 3a displays snapshots of the solution at six representative times and Fig. 3b shows the time evolution of the total tumor volume and its necrotic, hypoxic and proliferative regions. As pointed out before, due to the absence of better data, we started the simulation with initial conditions which are a rough estimate of what the situation might be in a tumor which is about to become malignant. Therefore, it is expected that the initial dynamics will be controlled by these conditions as indicated in Fig. 3b (see early times in the plot). During the initial period the tumor grows because there is nutrient available in its surroundings. The proliferative cells, however, become hypoxic driving the volume of proliferative tumor cells to zero. The time when we consider that the solution has evolved to a realistic initial scenario is marked with a vertical dashed line in Fig. 3b. Thereafter, because the nutrient transported by the initial capillary is not enough to feed the cancerous cells, the volume of the tumor remains almost constant for a time span of approximately one day. Struggling for survival, hypoxic tumor cells secrete TAFs to activate the angiogenesis cascade and enable further growth. As shown in Fig. 3a, around $t = 1.03$ days TAF reaches the initial capillary and a new sprout grows towards the tumor from the closest part of the pre-exiting capillary. Simultaneously, nutrients are released from the newly created vessels and diffuse into the surrounding tissue. As more TAF reaches the vessels, more capillaries develop and grow towards the tumor (see snapshot at $t = 1.47$ days). By the time the neovasculature reaches the tumor, the additional oxygen supply promotes tumor growth. The tumor plot at $t = 1.76$ days in Fig. 3b highlights the onset of the vascular phase of the tumor, in which a proliferative region starts to develop and the hypoxic region begins to shrink. The decrease in the hypoxic region's volume stems from two factors. On the one hand, the foremost capillaries provide sufficient nutrient to the outer tumor cells, turning hypoxia into normoxia. On the other hand, the necrotic core expands outward at the expense of the hypoxic region. As more capillaries break into the tumor (see snapshots at $t = 2.19$, $t = 2.65$ and $t = 3.02$

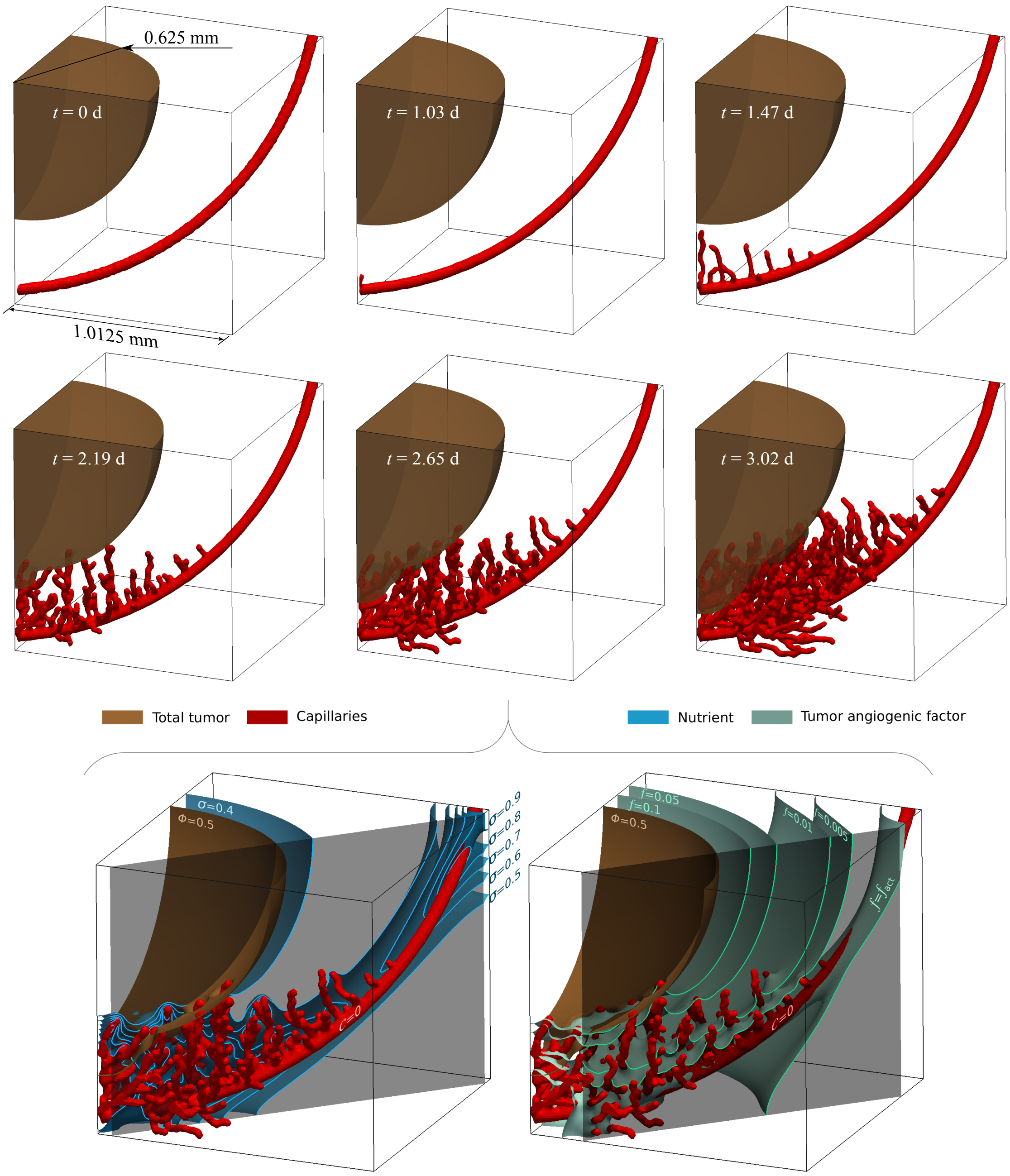

(a) The physical domain is a cube of side 2025 µm. Initially, there is a spherical tumor (brown) and a curved tubular capillary (red). Due to the existing symmetry, the actual simulation is performed on one octant of the tissue. We take $R = 8$. The panels in the first two rows show the evolution of the tumor and the capillaries. The bottom panels show details of the oxygen and TAF distributions at time $t = 2.65$ days. The plots show how the capillaries release nutrient and the tumor is directed toward oxygen-rich areas. It is also shown how TECs follow the gradients of TAF.

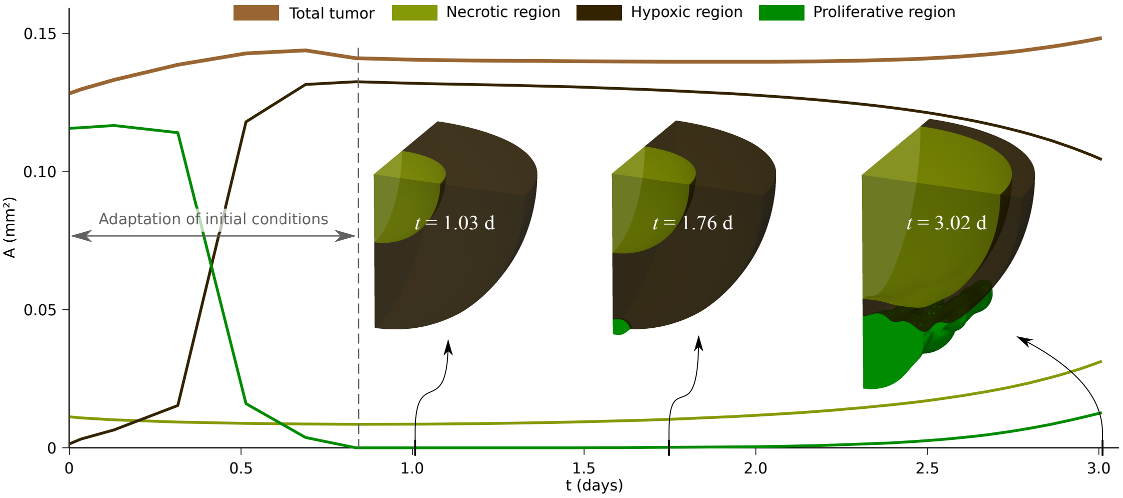

(b) Time evolution of the volume of the total tumoral mass, as well as the necrotic, hypoxic and proliferative regions. We consider that up to the dashed vertical line, the physics is highly influenced by the initial conditions, which are only a rough estimate of the biological situation at the initial time.

Figure 3. Coupled tumor growth and angiogenesis.

days in Fig. 3a), cancerous cells proliferate faster. Interestingly, the model predicts that the necrotic volume keeps increasing during the whole simulation and even accelerates its growth after angiogenesis has been triggered. This results from the fact that the nutrient released from the new vessels only reaches distances of ∼200 µm from its source due to nutrient uptake by surrounding cells. In addition, the velocity of TECs is lower inside the tumor (see Appendix A) than in the healthy tissue. This modeling choice tries to account for the well-known fact that the mechanical pressure is higher inside the tumor [84], which makes it harder for TECs to migrate. As a consequence, the nutrient is still insufficient inside tumor and more hypoxic tumor cells become necrotic at a rate similar to that of tumor growth.

Finally, the bottom panel of Fig. 3a shows details of the nutrient (left) and the TAF (right) concentrations at time $t = 2.65$ days. The left-hand side shows how the capillaries release nutrient and the tumor grows toward nutrient-rich areas. The right-hand side highlights how TAF emerges from the tumor and guides the chemotactic migration of TECs.

4.2. Vascular tumor growth in a macroscopic piece of colon tissue

In this section, we present the results of two- and three-dimensional simulations that aim at studying vascular tumor growth in realistic setups, in particular, in the geometry of a human colon tissue. The process undertaken to obtain such geometry is as follows: First, we obtained a histopathological image of the cross-section of a human colon [85]. Then, assuming that the outer radius of the colon is approximately 16 mm [86], we modified the normal histology cross-section such that it follows the curvature of the colon. The resulting image is shown in the central panel of Fig. 4. There, the gray-shaded region at the top right of the tissue represents our computational domain, whose dimensions are marked in the plot. As in this work we focus on early-stage colon cancer that has not yet invaded the mucosa layer, the computational domain only includes the mucosa and submucosa and it is bounded from bellow by the muscle layer (approximated by a circular arc). The top boundary, that is, the epithelium layer where colon cancer begins, presents a complex geometry. We approximated this curve using the Canny edge detection algorithm [87] and then

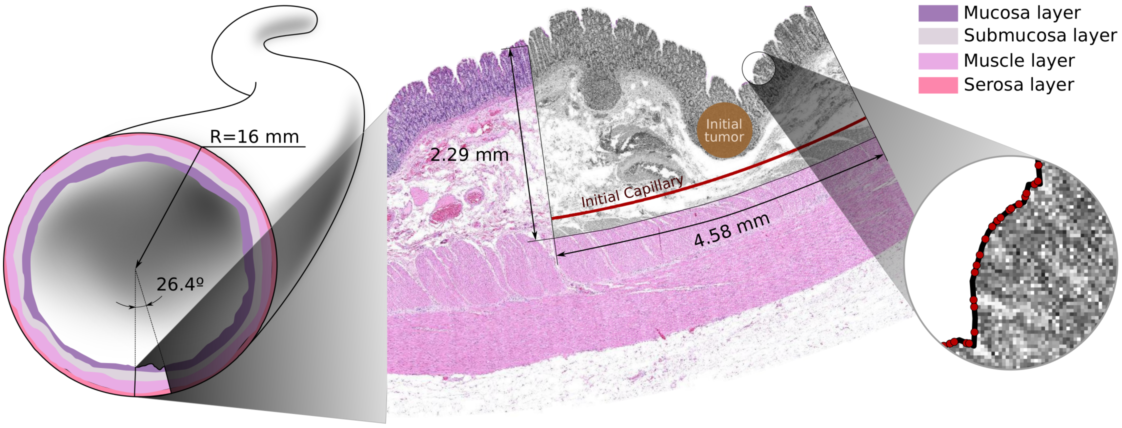

Figure 4. Vascular tumor growth in a macroscopic piece of colon tissue. The left-hand side shows a schematic view of a human colon, highlighting the different layers and the piece of tissue that we consider in our analysis. This area is zoomed-in in the central panel and shows a histopathological image of a colon section taken from [85]. Our simulation is performed in the gray region. The right plot shows an augmented image of the boundary of the domain and how we approximated it by a B-spline curve.

fitting a B-spline. We show in the figure a zoomed-in view where we represent the B-spline curve and its control points.

4.2.1. Two dimensional simulation

To begin the simulation we place a circular tumor (brown) with radius $R_t = 0.3$ mm in the mucosa layer of the tissue, as shown in Fig. 4. We assumed the existence of an initial capillary in the submucosa region. The capillary is a circular arc with a constant width of 25 µm. As in the previous case, the initial source of nutrient is the pre-existing capillary, where σ is set to 1. The central part of the tumor is assumed to have a concentric necrotic core of radius $R_n = 0.45R_t$. The mesh is composed by 640 C^1-quadratic elements in the radial direction and 960 C^1-quadratic elements in the circumferential direction.

As shown in the first row of Fig. 5, a new sprout grows from the initial capillary at $t = 2.8$ days. This occurs when the TAF released by hypoxic tumor cells reaches the capillary with a concentration higher than f_{act} (see Appendix A and the top left panel of Fig. 5 where the level set of the TAF concentration $f = f_{act}$ is shown). Then, the new capillaries migrate towards the gradient of TAF and the nutrient released from them diffuses in the surrounding tissue (not shown). Once the capillaries approach the tumor boundary, the tumor begins to grow (see snapshot at $t = 3.41$ days). As more capillaries grow, the tumor size increases significantly (see snapshots at $t = 3.93$ and $t = 4.28$ days). In the middle and bottom panels of Fig. 5, we observe that the necrotic region grows at the expense of the hypoxic area almost during the entire process. The proliferative region is practically absent from $t = 0.88$ to $t = 3.28$ days. Once the nutrient enters into the tumor, the proliferative region increases rapidly. At $t = 4.59$ the tumor area has increased by 37.5 %.

Fig. 5 shows that at the end of the simulation, the tumor is invading the submucosa layer. This is the point in which a pathologist would consider that the lesion is not a benign tumor, but a cancerous mass. It is expected that after this point, the tumor would try to invade the subsequent layers of the tissue and it would encounter mechanical opposition in its way. We believe that our model should be extended with a coupled biomechanical compartment to adequately account for this process [88–90].

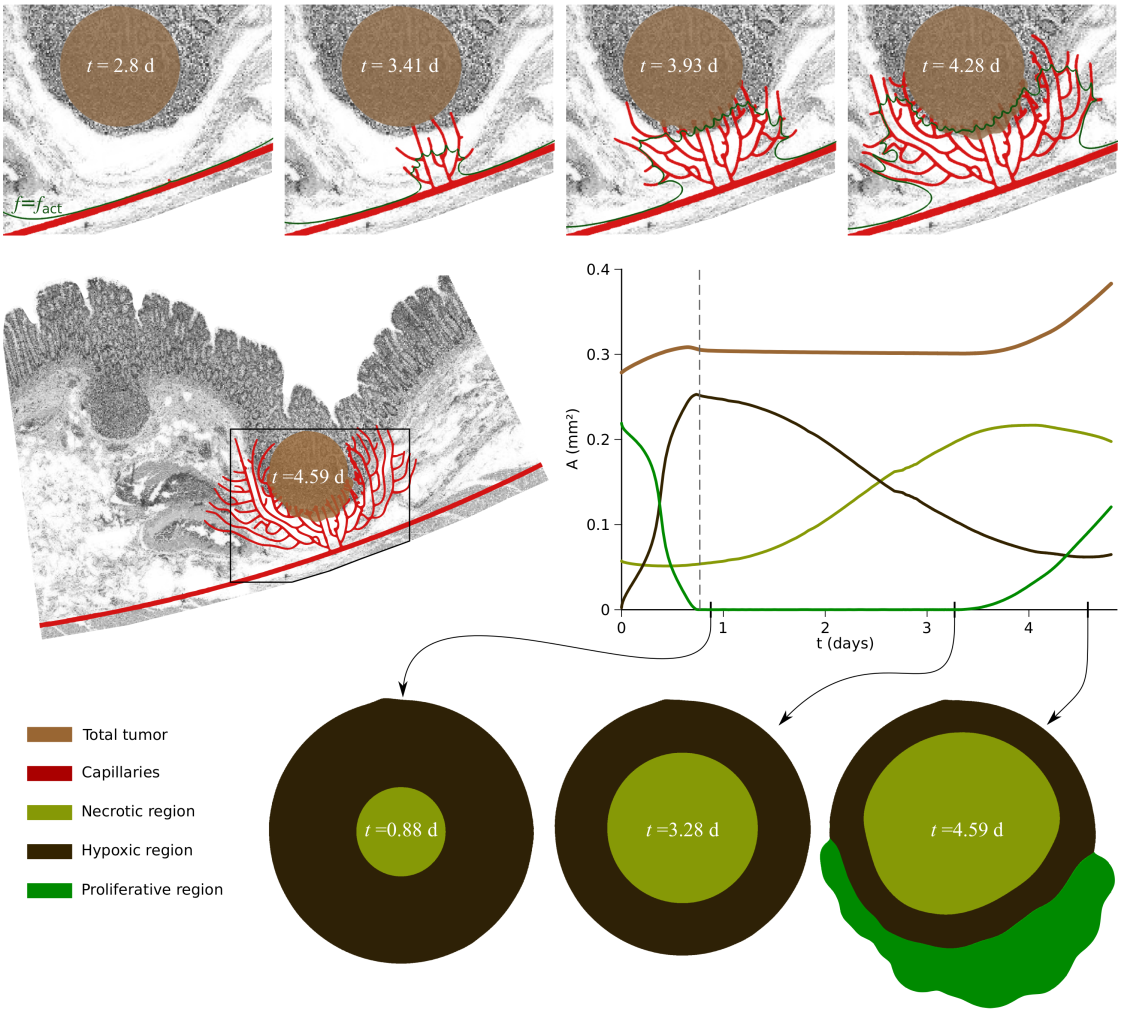

Figure 5. Vascular tumor growth in a macroscopic piece of colon tissue. Two-dimensional simulation. The mesh is composed of 960×640 C^1-quadratic elements. We take $\lambda_\phi = \sqrt{8}$ and $\lambda_c = 1$. The top row shows how the tumor recruits new capillaries by releasing TAF. The new capillaries provide nutrients that enable tumor growth. The right-hand side of the central row shows the time evolution of the volume of the total tumoral mass as well as its necrotic, hypoxic and proliferative regions. The accompanying pictures show the location of the different regions within the tumor.

4.2.2. Three-dimensional simulation

We generate the geometry by extruding the two-dimensional tissue 0.95 mm along the pipeline direction. We used a mesh composed by C^1-quadratic elements; 353 in the radial direction, 525 in the circumferential direction and 96 in the pipeline direction. This amounts to over 71 millions of unknowns that are evolved dynamically. As shown in the top left panel of Fig. 6, our initial conditions consist of two ellipsoidal tumors (brown) in the mucosa layer. The axes of the larger and smaller tumor are, respectively, $\{0.4, 0.5, 0.4\}$ and $\{0.12, 0.15, 0.12\}$. We did not have access to any data regarding the location of pre-existing vasculature at the initial time. Therefore, we created a three-layer lattice following the

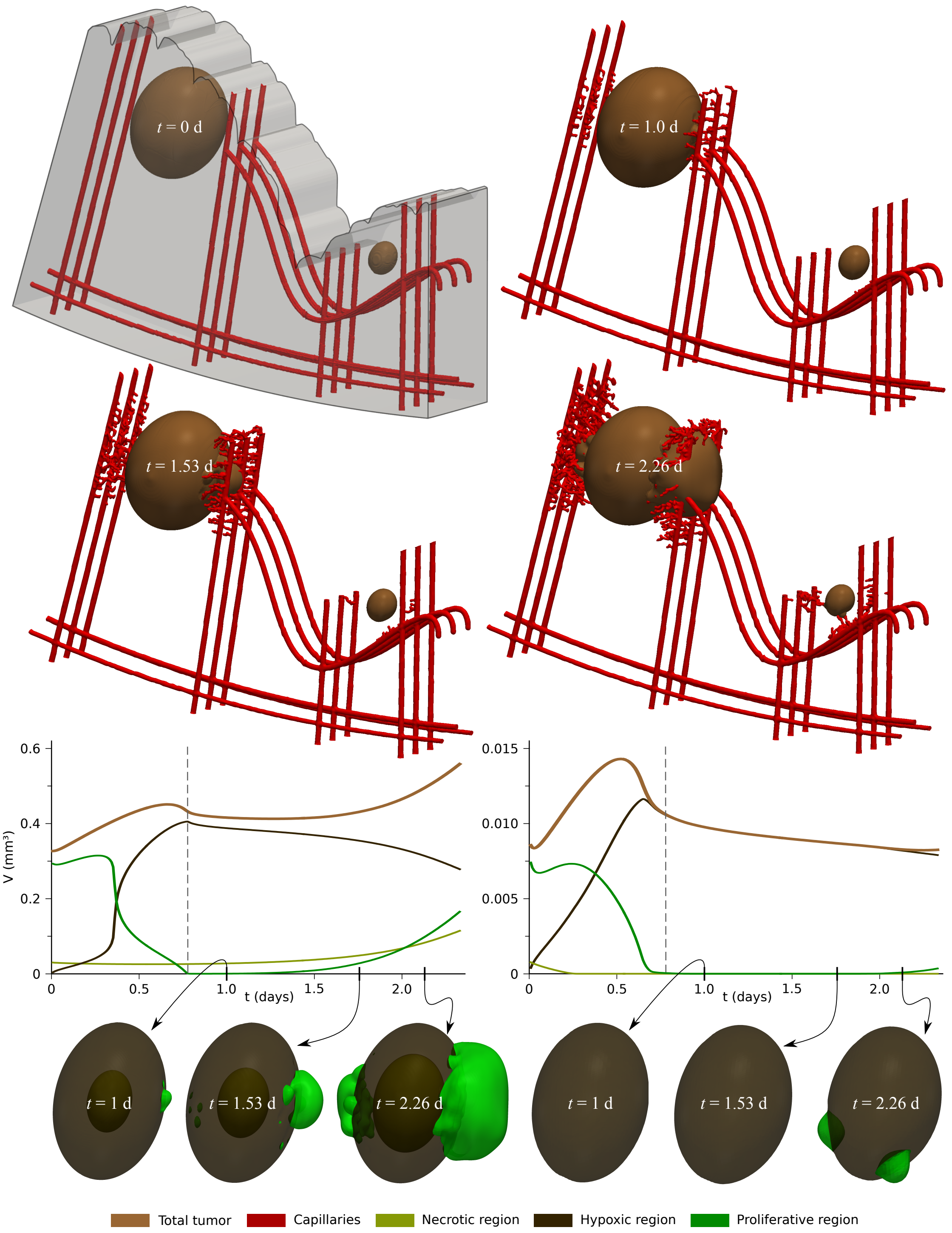

Figure 6. Vascular tumor growth in a macroscopic piece of colon tissue. Three-dimensional simulation. The mesh is composed of $353 \times 525 \times 96$ C^1-quadratic elements. We take $\lambda_\phi = 10$ and $R = 8$. Two ellipsoidal tumors are initially placed in the mucosa layer of the tissue. We also included several strips withs a constant radius of 25 µm representing the pre-existing vessels. We show snapshots of the solution (tumor and capillaries) at three representative times. The bottom panels show the time evolution of the total tumor mass as well as its necrotic, hypoxic and proliferative regions. The accompanying pictures show the spatial distribution of the different regions and the different dynamics exhibited by the small and the large tumor.

boundaries and the vertical direction of the computational domain, as shown in the plot.

We present several snapshots of the simulation showing the tumor and capillaries at $t = 1$, $t = 1.53$ and $t = 2.26$ days. At $t = 1$ day, several new sprouts grow towards the large tumor following the gradient of TAF. The growth of the big tumor, triggered by angiogenesis, has already started at this point, while the small tumor undergoes slight regression in the absence of enough nutrients to proliferate. As more TAF is secreted by the large tumor, the capillary network develops further; see the snapshot at time $t = 1.53$ days. This results in a rapid growth of the big tumor. By time $t = 2.26$ days, this tumor has provoked the advancement of hundreds of new capillaries. More importantly, the simulation reveals how the tumor co-opts new and parent capillaries as observed experimentally [91]. The small tumor, on the other hand has only promoted the growth of a few capillaries at the final time and is starting to show local clusters of proliferative cells at its bottom, highlighted in green at the bottom of Fig. 6.

The bottom panels of Fig. 6 present the time evolution of the volume of the different regions of the tumor. The bottom left and bottom right plots focus on the large and small tumor, respectively. After the early dynamics controlled by the initial conditions, the necrotic region of the big tumor grows. Note that the growth continues even after the neovasculature has significantly pervaded the tumor's microenvironment, which is a common experimental observation at the tissue scale. As observed in the plot, a significant part of the newly-created necrotic region grows at the expense of hypoxic cells. At $t = 1$ day, the tumor shows areas of localized proliferation, but such growth is small compared to the regression that takes place in other areas, which leads to mild global shrinkage of the tumor. At $t = 1.53$ days, proliferative regions are dominant and the tumor volume increases due to the amount of nutrient supplied by the newly-created capillaries. By the end of the simulation, at $t = 2.26$ days, the big tumor has increased its volume by approximately 54%.

The evolution of the small tumor, shown in the bottom right plot, presents two main differences when compared to that of the big tumor. The first difference is that the small tumor starts growing later than the larger tumor. The reason for this is that it takes longer for the small tumor to trigger angiogenesis because it is located farther away from the capillaries. Therefore, the distance that TAF needs to travel is longer. Once TAF has reached the pre-existent capillaries, the distance that new TECs need to bridge is also larger. The second difference is that the volume changes at a faster rate in the smaller tumor. This is a consequence of Eq. (1) representing surface-driven growth in the limit $\lambda_\phi \rightarrow 0$.

4.3. Angiogenesis restores normoxia in small tumor spheroids

In vivo experimental evidence shows that tumors may be quite heterogeneous, having simultaneously necrotic regions and areas with high vascular density [4, 92]. The numerical examples presented in Sect. 4.1 and Sect. 4.2 are in agreement with these observations as well as with the results of other simulations that consider discrete vascular networks [31, 57]. This is in contrast with recent *in vitro* experiments that show the complete disappearance of the necrotic region after vascularization in tumor spheroids [83]. A key difference of the latter experiment, compared to the observations reported in [4] is the size of the tumors. In reference [83] the experiments are performed with tumor spheroids of radius ~200 µm, while the *in vivo* evidence refers to larger tumors. The goal of this numerical example is to show that our model not only predicts large necrotic areas in large tumors (shown in Sects. 4.1 and 4.2), but also the restoration of normoxia after vascularization in small tumors.

To illustrate this point, we perform a computation on a cubic tissue of side 775 µm. Mimicking the experiment in [83], we place an initially spherical tumor with radius 200 µm at the center of the domain and a small capillary in its environment. To reduce the computational cost, we make use of the symmetry and utilize only one octant of the physical domain. The mesh is composed of 64 C^1-quadratic elements in each direction. Initially, we assume the presence of a concentric necrotic core in the tumor with radius 100 µm (see bottom panel of Fig. 7), where we set $\sigma = 0$.

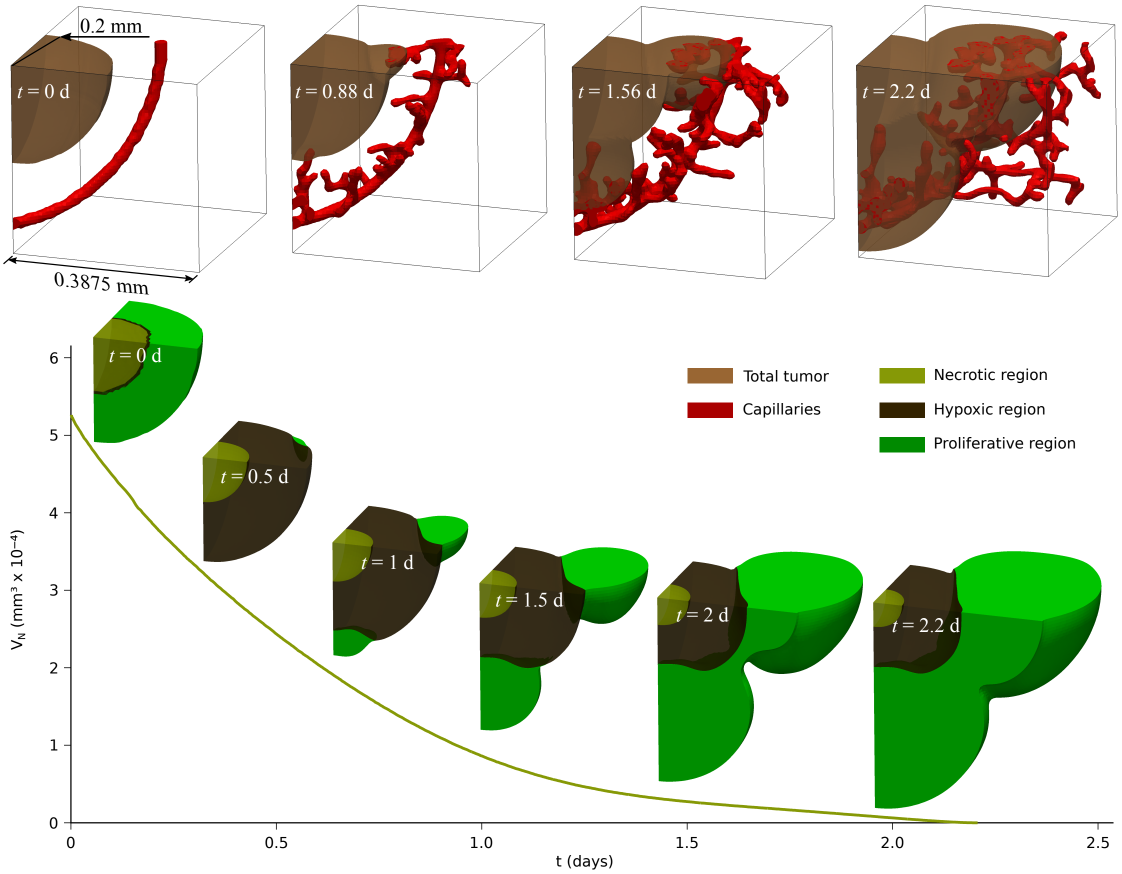

Figure 7. Angiogenesis restores normoxia in small tumor spheroids. The whole domain of the problem represents a cubic tissue of side 775 μm with a spherical tumor (brown) at its center and a curved tubular capillary (red) in its surroundings. The simulation is performed on one octant of the tissue using a uniform mesh of 64^3 C^1-quadratic elements. We take $\sigma^0_{\mathrm{ecm}} = 0.42$. The top row shows the evolution of the tumor and the capillaries. The bottom row shows the time evolution of the volume of the necrotic region. The accompanying pictures present the spatial distribution of the necrotic, hypoxic and proliferative regions of the tumor. The simulation shows how angiogenesis restores normoxia in small tumor spheroids.

At the initial stage ($t < 0.5$ days), the pre-existing nutrient is consumed by the tumor and becomes insufficient to maintain the proliferative cells. Therefore, the hypoxic volume increases rapidly. The proliferative region is almost absent at $t = 0.5$ days. At this point, the neovasculature reaches the tumor and enables localized growth of proliferative cells at the contact areas. As new capillaries grow ($t > 1$ day) the trend persists and the necrotic core keeps decreasing. Eventually, the necrotic area has vanished at $t \approx 2.3$ days.

5. Conclusions

We presented a phenomenological model that accounts for the coupled growth of tumors and their associated vasculature in three dimensions trying to describe the onset of malignancy in solid tumors. By developing a suitable computational method based on isogeometric analysis, we have been able to perform two- and three-dimensional computations that aim at mimicking experimental setups at relatively large scales (~1 cm^3). In particular, we have computed coupled tumor growth and angiogenesis on the geometry of a human colon taken from a histopathological image. The model reproduces several experimental observations at different scales. As an example, the simulations show how new vessels sprout from the pre-existing vasculature and grow towards the tumor, providing a source of nutrients that enables further growth. The model also shows how the neovasculature is able to restore normoxia in small tumor spheroids but not in larger tumors, as observed in experiments. Although we believe that this paper opens a number of opportunities for future research in the computational mechanics community, our approach presents some limitations that should be addressed in the future. For example, our model should be extended with a biomechanical compartment that permits understanding how the tumor invades the submucosa and muscle layers. In this process, the tumor will experience opposing mechanical forces that might favor its expansion towards the luminal space of the colon. Our model only accounts for a generic tumor angiogenic factor that represents a balance between pro- and anti-angiogenic substances. It would be interesting to account for pro- and anti-angiogenic factors explicitly. Using discrete agents to model the earliest stages of metastasis is a challenging but potentially interesting research topic. Another avenue for future research is to model explicitly blood flow in the capillaries. This will lead to a more realistic description of the nutrient release by capillaries.

6. Acknowledgments

This work was supported by the European Research Council through the FP7 Ideas Starting Grant program (Contract # 307201). This support is gratefully acknowledged.

Appendix A. Details of the model

In Eq. (1), M_ϕ is defined as

$$M_\phi(\sigma) = M_{\text{ref}}\mathcal{H}(\sigma - \sigma^{h-v}) \tag{A.1}$$

where $\mathcal{H}$ is a smoothed-out Heaviside function. In Eq. (4), the proliferation rate of endothelial cells $\mathcal{B}_p(f)$ is defined as

$$\mathcal{B}_p(f) = \begin{cases} B_p f & \text{if } f < f_p \\ B_p f_p & \text{if } f \geq f_p \end{cases}, \tag{A.2}$$

where B_p and f_p are constant parameters. In Eq. (5), the rate of TAF production by tumor cells is controlled by the function $\mathcal{G}(\sigma)$, which is defined as

$$\mathcal{G}(\sigma) = \mathcal{G}_{\text{ref}} \exp\left(- \left(\frac{\sigma - (\sigma^{n\text{-}h} + \sigma^{h\text{-}v})/2}{\sigma^G_{\text{ref}}} \right)^2 \right), \tag{A.3}$$

This completes the definition of the continuous equations of the model.

In what follows, we describe how the discrete agents that represent TECs are created/eliminated and migrate throughout the tissue. Tip endothelial cells are modeled as circular or spherical agents of radius R in two and three dimensions, respectively. For example, in three dimensions this implies that if a new TEC is created at a particular point, a spherical volume of radius R centered at that point is defined. The continuous variable c is set to 1 in that volume using the concept of templates [42]. A new agent representing a TEC is created at a point if the following three conditions are simultaneously satisfied at that point

1. $c \geq c_{act}$,
2. $f \geq f_{act}$ and
3. $d_{min} > \delta_4$.

Here, c_{act}, f_{act} and δ_4 are constants. The first condition guarantees that new TECs are created at a vessel, where endothelial cells are located. The second condition reflects the biological behavior whereby endothelial cells which are reached by TAF at a sufficiently high concentration change their phenotype and become migratory. In the third condition, d_{min} is the distance of the point to the closest TEC. This condition mimics the lateral inhibition mechanism and prevents the network from becoming too dense [15]. Once TECs are created they can migrate, while the above-mentioned conditions are satisfied at its center. If at some point these conditions fail to be satisfied at the TEC center, the agent gets deactivated.

Active TECs migrate following gradients of TAF. In particular, the velocity of a TEC is given by

$$\boldsymbol{v} = \chi \frac{\nabla f}{|\nabla f|} \mathcal{J}(\phi), \tag{A.4}$$

where χ is a constant and $\mathcal{J}(\phi) = 0.9\mathcal{H}(1/2 - \phi) + 0.1$. The function $\mathcal{J}$ introduces into the model the experimental observation that TECs migrate more slowly inside a tumor than in healthy tissue due to the higher pressure in the cancerous mass. In particular, $\mathcal{J}$ takes the value ~ 1 outside the tumor and ~ 0.1 inside. In addition to chemotactic motion, when TECs have migrated more than four times their radius away from their parent vessel, a set of points is checked in the TEC's neighborhood. If the value of c at any of these points is positive, then it means that there is a nearby capillary and the TEC velocity is modified so as to migrate towards that capillary. This feature of the model is implemented to mimic the filopodia of TECs, which produces a similar effect to increase the connectivity of the network and enhance blood flow.

Parameter	Description	Unit	*In silico* value
M_{ref}	Reference mobility of the tumor	$[\mathrm{T}^{-1}]$	0.35
λ_ϕ	Interface width of tumor	[L]	$\sqrt{20}$
ϵ	Parameter of the tilting function	[-]	0.01
M_c	Mobility of endothelial cells	$[\mathrm{L}^2\mathrm{T}^{-1}]$	1
λ_c	Interface width of capillaries	[L]	$\sqrt{6}$
B_p	Proliferation rate of endothelial cells	$[\mathrm{T}^{-1}]$	1.401
f_p	TAF threshold for highest proliferation	[-]	0.3
D_f	Diffusion coefficient of TAF	$[\mathrm{L}^2\mathrm{T}^{-1}]$	100
B_u	Uptake rate of TAF by capillaries	$[\mathrm{T}^{-1}]$	6.25
$\sigma^{n\text{-}h}$	Necrotic/hypoxic nutrient threshold	[-]	0.2
$\sigma^{h\text{-}v}$	Hypoxic/viable nutrient threshold	[-]	0.4
σ^{m}_{ref}	Reference nutrient concentration for the tilting function	[-]	0.067
σ^{G}_{ref}	Reference nutrient concentration for the TAF production function	[-]	$1/\sqrt{125}$
G_{ref}	Reference value for TAF production rate	$[\mathrm{T}^{-1}]$	0.008
D_σ	Diffusion coefficient of the nutrient	$[\mathrm{L}^2\mathrm{T}^{-1}]$	30
V^c_p	Production rate of nutrient	$[\mathrm{T}^{-1}]$	1
V^T_u	Uptake rate of nutrient by tumor	$[\mathrm{T}^{-1}]$	0.006
V^H_u	Uptake rate of nutrient by host tissue	$[\mathrm{T}^{-1}]$	0.0006
R	TEC radius	[L]	5
c_{act}	Condition 1 for TEC (de)activation	[-]	0.9
f_{act}	Condition 2 for TEC (de)activation	[-]	0.001
χ	Chemotatic constant	$[\mathrm{L}\mathrm{T}^{-1}]$	7.28
δ_4	Dll4 effective distance	[L]	80

Table A.1. *In silico* values of the parameters used in the proposed model. Parameters related to angiogenesis are obtained from [42]. The physical values of the parameters may be obtained using the length scale $L_s = 1.25\,\mu\text{m}$ and time scale $T_s = 1562.5$ s.

References

[1] D. Hanahan, R. A. Weinberg, Hallmarks of cancer: The next generation, Cell 144 (2011) 646–674.

[2] R. Weinberg, One renegade cell: How cancer begins, Basic Books, 1998.

[3] J. Folkman, Tumor angiogenesis: therapeutic implications, N. Engl. J. Med. (1971) 1182–6.

[4] M. Höckel, P. Vaupel, Tumor hypoxia: definitions and current clinical, biologic, and molecular aspects, JNCI-J. Natl. Cancer Inst. 93 (2001) 266–276.

[5] P. Vaupel, L. Harrison, Tumor hypoxia: causative factors, compensatory mechanisms, and cellular response, The oncologist 9 (2004) 4–9.

[6] D. J. Hicklin, L. M. Ellis, Role of the vascular endothelial growth factor pathway in tumor growth and angiogenesis, J. Clin. Oncol. 23 (2005) 1011–1027.

[7] A. Beenken, M. Mohammadi, The FGF family: biology, pathophysiology and therapy, Nat. Rev. Drug. Discov. 8 (2009) 235–253.

[8] B. L. Krock, N. Skuli, M. C. Simon, Hypoxia-induced angiogenesis good and evil, Genes & cancer 2 (2011) 1117–1133.

[9] M. L. Iruela-Arispe, M. Lombardo, H. C. Krutzsch, J. Lawler, D. D. Roberts, Inhibition of angiogenesis by thrombospondin-1 is mediated by 2 independent regions within the type 1 repeats, Circulation 100 (1999) 1423–1431.

[10] M. Potente, H. Gerhardt, P. Carmeliet, Basic and therapeutic aspects of angiogenesis, Cell 146 (2011) 873–887.

[11] P. Carmeliet, R. K. Jain, Molecular mechanisms and clinical applications of angiogenesis, Nature 473 (2011) 298–307.

[12] S. M. Weis, D. A. Cheresh, Tumor angiogenesis: molecular pathways and therapeutic targets., Nature Medicine 17 (2011) 1359–1370.

[13] S. P. Herbert, D. Y. R. Stainier, Molecular control of endothelial cell behaviour during blood vessel morphogenesis, Nat. Rev. Mol. Cell Biol. 12 (2011) 551–564.

[14] S. P. Herbert, J. Y. M. Cheung, D. Y. R. Stainier, Determination of endothelial stalk versus tip cell potential during angiogenesis by H2.0-like homeobox-1, Curr. Biol. 22 (2012) 1789–1794.

[15] M. Hellström, L.-K. Phng, J. J. Hofmann, E. Wallgard, L. Coultas, P. Lindblom, J. Alva, A.-K. Nilsson, L. Karlsson, N. Gaiano, et al., Dll4 signalling through notch1 regulates formation of tip cells during angiogenesis, Nature 445 (2007) 776–780.

[16] H. Gerhardt, M. Golding, M. Fruttiger, C. Ruhrberg, A. Lundkvist, A. Abramsson, M. Jeltsch, C. Mitchell, K. Alitalo, D. Shima, C. Betsholtz, VEGF guides angiogenic sprouting utilizing endothelial tip cell filopodia, J. Cell Biol. 161 (2003) 1163–1177.

[17] L. A. Torre, F. Bray, R. L. Siegel, J. Ferlay, J. Lortet-Tieulent, A. Jemal, Global cancer statistics, 2012, CA: A Cancer Journal for Clinicians 65 (2015) 87–108.

[18] R. Siegel, C. DeSantis, A. Jemal, Colorectal cancer statistics, 2014, CA: A Cancer Journal for Clinicians 64 (2014) 104–117.

[19] G. Giordano, A. Febbraro, M. Venditti, S. Campidoglio, N. Olivieri, K. Raieta, P. Parcesepe, G. C. Imbriani, A. Remo, M. Pancione, Targeting angiogenesis and tumor microenvironment in metastatic colorectal cancer: Role of aflibercept, Gastroenterology Research and Practice 2014 (2014) 526178.

[20] T. J. Saclarides, Angiogenesis in colorectal cancer, Surgical Clinics of North America 77 (1997) 253 – 260.

[21] S. B. Edge, D. R. Byrd, C. C. Compton, A. G. Fritz, F. L. Greene, A. Trotti (Eds.), AJCC cancer staging manual, NY: Springer, 2010.

[22] J. S. Lowengrub, H. B. Frieboes, F. Jin, Y.-L. Chuang, X. Li, P. Macklin, S. M. Wise, V. Cristini, Nonlinear modelling of cancer: Bridging the gap between cells and tumours, Nonlinearity 23 (2010) R1–R9.

[23] G. Sciumè, W. Gray, M. Ferrari, P. Decuzzi, B. Schrefler, On computational modeling in tumor growth, Arch. Comput. Method Eng. 20 (2013) 327–352.

[24] J. T. Oden, E. A. B. F. Lima, R. C. Almeida, Y. Feng, M. N. Rylander, D. Fuentes, D. Faghihi, M. M. Rahman, M. DeWitt, M. Gadde, J. C. Zhou, Toward predictive multiscale modeling of vascular tumor growth, Arch. Comput. Method Eng. (2015) 1–45.

[25] J. Sinek, H. B. Frieboes, X. Zheng, V. Cristini, Two-dimensional chemotherapy simulations demonstrate fundamental transport and tumor response limitations involving nanoparticles, Biomed. Microdevices 6 (2004) 297–309.

[26] X. Zheng, S. M. Wise, V. Cristini, Nonlinear simulation of tumor necrosis, neo-vascularization and tissue invasion via an adaptive finite-element/level-set method, Bull. Math. Biol. 67 (2005) 211–259.

[27] A. R. A. Anderson, M. A. J. Chaplain, A mathematical model for capillary network formation in the absence of endothelial cell proliferation, Appl. Math. Lett. 11 (1998) 109–114.

[28] C. S. Hogea, B. T. Murray, J. A. Sethian, Simulating complex tumor dynamics from avascular to vascular growth using a general level-set method, J. Math. Biol. 53 (2006) 86–134.

[29] L. Zhang, C. A. Athale, T. S. Deisboeck, Development of a three-dimensional multiscale agent-based tumor model: simulating gene-protein interaction profiles, cell phenotypes and multicellular patterns in brain cancer, J. Theor. Biol. 244 (2007) 96–107.

[30] H. B. Frieboes, J. S. Lowengrub, S. M. Wise, X. Zheng, P. Macklin, E. L. Bearer, V. Cristini, Computer simulation of glioma growth and morphology, Neuroimage 37 (2007) S59–S70.

[31] H. B. Frieboes, F. Jin, Y.-L. Chuang, S. M. Wise, J. S. Lowengrub, V. Cristini, Three-dimensional multispecies nonlinear tumor growth-II: tumor invasion and angiogenesis, J. Theor. Biol. 264 (2010) 1254–1278.

[32] E. L. Bearer, J. S. Lowengrub, H. B. Frieboes, Y.-L. Chuang, F. Jin, S. M. Wise, M. Ferrari, D. B. Agus, V. Cristini, Multiparameter computational modeling of tumor invasion, Cancer Res. 69 (2009) 4493–4501.

[33] V. Cristini, X. Li, J. S. Lowengrub, S. M. Wise, Nonlinear simulations of solid tumor growth using a mixture model: invasion and branching, J. Math. Biol. 58 (2009) 723–763.

[34] A. Shirinifard, J. S. Gens, B. L. Zaitlen, N. J. Popławski, M. Swat, J. A. Glazier, 3D multi-cell simulation of tumor growth and angiogenesis, PLoS ONE 4 (2009) e7190.

[35] H. Perfahl, H. M. Byrne, T. Chen, V. Estrella, T. Alarcón, A. Lapin, R. A. Gatenby, R. J. Gillies, M. C. Lloyd, P. K. Maini, M. Reuss, M. R. Owen, Multiscale modelling of vascular tumour growth in 3D: the roles of domain size and boundary conditions, PLoS ONE 6 (2011) e14790.

[36] M. Welter, H. Rieger, Interstitial fluid flow and drug delivery in vascularized tumors: A computational model, PLoS ONE 8 (2013) e70395.

[37] L. Tang, A. L. van de Ven, D. Guo, V. Andasari, V. Cristini, K. C. Li, X. Zhou, Computational modeling of 3D tumor growth and angiogenesis for chemotherapy evaluation, PLoS One 9 (2014) e83962.

[38] J. T. Oden, A. J. Hawkins-Daarud, S. Prudhomme, General diffuse-interface theories and an approach to predictive tumor growth modeling, Math. Models Methods Appl. Sci. 20 (2010) 477–517.

[39] E. A. B. F. Lima, J. T. Oden, R. C. Almeida, A hybrid ten-species phase-field model of tumor growth, Math. Models Methods Appl. Sci. 24 (2014) 2569–2599.

[40] T. S. Deisboeck, Z. Wang, P. Macklin, V. Cristini, Multiscale cancer modeling, Annu. Rev. Biomed. Eng. 13 (2011).

[41] R. D. M. Travasso, E. C. Poiré, M. Castro, J. C. Rodríguez-Manzaneque, A. Hernández-Machado, Tumor angiogenesis and vascular patterning: A mathematical model, PLoS One 6 (2011) e19989.

[42] G. Vilanova, I. Colominas, H. Gomez, Capillary networks in tumor angiogenesis: From discrete endothelial cells to phase-field averaged descriptions via isogeometric analysis, Int. J. Numer. Meth. Biomed. 29 (2013) 1015–1037.

[43] J. Xu, G. Vilanova, H. Gomez, A mathematical model coupling tumor growth and angiogenesis, PLoS ONE 53 (2016) 449–464.

[44] L.-Q. Chen, Phase-field models for microstructure evolution, Annu. Rev. Mater. Sci. 32 (2002) 113–140.

[45] R. Kobayashi, A brief introduction to phase field method, volume 1270, Dalian, pp. 282–291. Conference of 14th International Summer School on Crystal Growth, ISSCG14.

[46] L. M. Pismen, Patterns and interfaces in dissipative dynamics, Springer Science & Business Media, 2006.

[47] W. J. Boettinger, J. A. Warren, C. Beckermann, A. Karma, Phase-field simulation of solidification, Ann. Rev. Mater. Res. 32 (2002) 163–194.

[48] I. Steinbach, Phase-field models in materials science, Model. Simul. Mater. Sci. Eng. 17 (2009) 073001.

[49] A. Karma, D. A. Kessler, H. Levine, Phase-field model of mode III dynamic fracture, Phys. Rev. Lett. 87 (2001) 045501.

[50] M. J. Borden, C. V. Verhoosel, M. A. Scott, T. J. R. Hughes, C. M. Landis, A phase-field description of dynamic brittle fracture, Comput. Meth. Appl. Mech. Eng. 217 (2012) 77–95.

[51] M. J. Borden, T. J. R. Hughes, C. M. Landis, C. V. Verhoosel, A higher-order phase-field model for brittle fracture: Formulation and analysis within the isogeometric analysis framework, Comput. Meth. Appl. Mech. Eng. 273 (2014) 100–118.

[52] Q. Du, M. Li, C. Liu, Analysis of a phase field Navier-Stokes vesicle-fluid interaction model, Discrete Contin. Dyn. Syst. Ser. B 8 (2007) 539.

[53] J. Bueno, C. Bona-Casas, Y. Bazilevs, H. Gomez, Interaction of complex fluids and solids: theory, algorithms and application to phase-change-driven implosion, Comput. Mech. 55 (2015) 1105–1118.

[54] K. R. Elder, N. Provatas, J. Berry, P. Stefanovic, M. Grant, Phase-field crystal modeling and classical density functional theory of freezing, Phys. Rev. B 75 (2007) 064107.

[55] L. Chen, J. Chen, R. A. Lebensohn, Y. Z. Ji, T. W. Heo, S. Bhattacharyya, K. Chang, S. Mathaudhu, Z. K. Liu, L.-Q. Chen, An integrated fast fourier transform-based phase-field and crystal plasticity approach to model recrystallization of three dimensional polycrystals, Comput. Meth. Appl. Mech. Eng. 285 (2015) 829–848.

[56] J. Bueno, I. Starodumov, H. Gomez, P. Galenko, D. Alexandrov, Three dimensional structures predicted by the modified phase field crystal equation, Comput. Mater. Sci. 111 (2016) 310–312.

[57] S. M. Wise, J. S. Lowengrub, H. B. Frieboes, V. Cristini, Three-dimensional multispecies nonlinear tumor growth-I: model and numerical method, J. Theor. Biol. 253 (2008) 524–543.

[58] J. T. Oden, E. E. Prudencio, A. J. Hawkins-Daarud, Selection and assessment of phenomenological models of tumor growth, Math. Models Methods Appl. Sci. 23 (2013) 1309–1338.

[59] A. J. Hawkins-Daarud, K. G. van der Zee, J. T. Oden, Numerical simulation of a thermodynamically consistent four-species tumor growth model, International journal for numerical methods in biomedical engineering 28 (2012) 3–24.

[60] A. J. Hawkins-Daarud, S. Prudhomme, K. G. van der Zee, J. T. Oden, Bayesian calibration, validation, and uncertainty quantification of diffuse interface models of tumor growth, J. Math. Biol. 67 (2013) 1457–1485.

[61] H. Gomez, K. G. van der Zee, Computational phase-field modeling, Encyclopedia of Computational Mechanics (2016).

[62] A. D. Conger, M. C. Ziskin, Growth of mammalian multicellular tumor spheroids, Cancer research 43 (1983) 556–560.

[63] K. Ellem, G. Kay, The nature of conditioning nutrients for human malignant melanoma cultures, Journal of cell science 62 (1983) 249–266.

[64] G. Vilanova, Mathematical modeling and numerical simulation of tumor angiogenesis, Ph.D. thesis, Universidade da Coruña, 2016.

[65] A. Ramanathan, C. Wang, S. L. Schreiber, Perturbational profiling of a cell-line model of tumorigenesis by using metabolic measurements, Proc. Natl. Acad. Sci. 102 (2005) 5992–5997.

[66] G. Thurston, I. Noguera-Troise, G. D. Yancopoulos, The delta paradox: Dll4 blockade leads to more tumour vessels but less tumour growth, Nat. Rev. Cancer 7 (2007) 327–331.

[67] S. Shan, A. C. Lockhart, W. Y. Saito, A. M. Knapp, K. R. Laderoute, M. W. Dewhirst, The novel tubulin-binding drug BTO-956 inhibits R3230Ac mammary carcinoma growth and angiogenesis in fischer 344 rats, Clin. Cancer Res. 7 (2001) 2590–2596.

[68] T. J. R. Hughes, J. A. Cottrell, Y. Bazilevs, Isogeometric analysis: CAD, finite elements, NURBS, exact geometry and mesh refinement, Comput. Meth. Appl. Mech. Eng. 194 (2005) 4135–4195.

[69] J. A. Cottrell, T. J. R. Hughes, A. Reali, Studies of refinement and continuity in isogeometric structural analysis, Comput. Meth. Appl. Mech. Eng. 196 (2007) 4160–4183.

[70] Y. Bazilevs, V. M. Calo, J. A. Cottrell, J. A. Evans, T. J. R. Hughes, S. Lipton, M. A. Scott, T. W. Sederberg, Isogeometric analysis using T-splines, Comput. Meth. Appl. Mech. Eng. 199 (2010) 229–263.

[71] D. Schillinger, L. Dedè, M. A. Scott, J. A. Evans, M. J. Borden, E. Rank, T. J. R. Hughes, An isogeometric design-through-analysis methodology based on adaptive hierarchical refinement of NURBS, immersed boundary methods, and T-spline cad surfaces, Comput. Meth. Appl. Mech. Eng. 249-252 (2012) 116–150.

[72] J. A. Cottrell, T. J. R. Hughes, Y. Bazilevs, Isogeometric analysis: toward integration of CAD and FEA, John Wiley & Sons, 2009.

[73] F. Auricchio, L. Beirão da Veiga, T. J. R. Hughes, A. Reali, G. Sangalli, Isogeometric collocation for elastostatics and explicit dynamics, Comput. Meth. Appl. Mech. Eng. 249-252 (2012) 2–14.

[74] H. Casquero, L. Liu, Y. Zhang, A. Reali, H. Gomez, Isogeometric collocation using analysis-suitable T-splines of arbitrary degree, Comput. Meth. Appl. Mech. Eng. 301 (2016) 164 – 186.

[75] A. Reali, H. Gomez, An isogeometric collocation approach for bernoulli–euler beams and kirchhoff plates, Comput. Meth. Appl. Mech. Eng. 284 (2015) 623–636.

[76] H. Gomez, L. De Lorenzis, The variational collocation method, Computer Methods in Applied Mechanics and Engineering (2016).

[77] H. Gomez, V. M. Calo, Y. Bazilevs, T. J. R. Hughes, Isogeometric analysis of the Cahn–Hilliard phase-field model, Comput. Meth. Appl. Mech. Eng. 197 (2008) 4333–4352.

[78] H. Gomez, T. J. R. Hughes, X. Nogueira, V. M. Calo, Isogeometric analysis of the isothermal Navier-Stokes-Korteweg equations, Comput. Meth. Appl. Mech. Eng. 199 (2010) 1828–1840.

[79] H. Gomez, J. París, Numerical simulation of asymptotic states of the damped Kuramoto-Sivashinsky equation, Phys. Rev. E 83 (2011) 046702.

[80] H. Gomez, T. J. R. Hughes, Provably unconditionally stable, second-order time-accurate, mixed variational methods for phase-field models, J. Comput. Phys. 230 (2011) 5310 – 5327.

[81] H. Gomez, X. Nogueira, An unconditionally energy-stable method for the phase field crystal equation, Comput. Meth. Appl. Mech. Eng. 249-252 (2012) 52–61.

[82] K. E. Jansen, C. H. Whiting, G. M. Hulbert, A generalized-α method for integrating the filtered Navier-Stokes equations with a stabilized finite element method, Comput. Meth. Appl. Mech. Eng. 190 (2000) 305 – 319.

[83] M. Wartenberg, F. Dönmez, F. C. Ling, H. Acker, J. Hescheler, H. Sauer, Tumor-induced angiogenesis studied in confrontation cultures of multicellular tumor spheroids and embryoid bodies grown from pluripotent embryonic stem cells, The FASEB Journal 15 (2001) 995–1005.

[84] C.-H. Heldin, K. Rubin, K. Pietras, A. Östman, High interstitial fluid pressure - an obstacle in cancer therapy, Nat. Rev. Cancer 4 (2004) 806–813.

[85] M. Shetiwy, GI Pathology–Neoplastic Small Bowel and Colon, www.studyblue.com, 2013.

[86] A. Herold, P.-A. Lehur, K. E. Matzel, P. O'Connell, Coloproctology, Springer-Verlag, 2008.

[87] J. Canny, A computational approach to edge detection, IEEE Transactions on pattern analysis and machine intelligence (1986) 679–698.

[88] C. M. Edwards, S. J. Chapman, Biomechanical modelling of colorectal crypt budding and fission, Bull. Math. Biol. 69 (2007) 1927–1942.

[89] J. A. Weis, M. I. Miga, L. R. Arlinghaus, X. Li, V. Abramson, A. B. Chakravarthy, P. Pendyala, T. E. Yankeelov, Predicting the response of breast cancer to neoadjuvant therapy using a mechanically coupled reaction–diffusion model, Cancer Res. 75 (2015) 4697–4707.

[90] K. C. L. Wong, R. M. Summers, E. Kebebew, J. Yao, Tumor growth prediction with reaction-diffusion and hyperelastic biomechanical model by physiological data fusion, Med. Image Anal. 25 (2015) 72–85.

[91] J. Holash, P. C. Maisonpierre, D. Compton, P. Boland, C. R. Alexander, D. Zagzag, G. D. Yancopoulos, S. J. Wiegand, Vessel cooption, regression, and growth in tumors mediated by angiopoietins and VEGF, Science 284 (1999) 1994–1998.

[92] A. L. Harris, Hypoxia - a key regulatory factor in tumour growth, Nat. Rev. Cancer 2 (2002) 38–47.